POLITECNICO DI MILANO

Scuola di Ingegneria Industriale e dell'Informazione

Corso di Laurea Magistrale in Ingegneria Biomedica

GMM-based vascular segmentation method for 3D CBCT DSA brain images for SEEG planning in epilepsy surgery

Relatore: Prof. Elena De Momi

Correlatore: Ing. Davide Scorza

Tesi di Laurea Magistrale di:

Andrea Ghilardi (matr. 836868)

Anno Accademico 2016/2017

Ringraziamenti

I miei più sinceri ringraziamenti vanno alla professoressa Elena De Momi, per avermi proposto questo progetto di tesi e avermi dato la possibilità di fare esperienza in un'azienda d'avanguardia nel settore della robotica medica.

A Davide Scorza, correlatore, tutor e amico, che mi ha supportato e fornito preziosi consigli per affrontare le difficoltà incontrate durante questo percorso e per il futuro lavorativo.

Alla mia famiglia, che mi ha permesso di seguire i miei sogni, mi ha supportato e ha sempre creduto in me.

Infine, ma non in ordine di importanza, a Giulia, mio sostegno e guida, che con il suo amore sincero mi ha fatto capire che non esiste limite ai nostri sogni e che solo con l'impegno e la felicità nel cuore è possibile raggiungerli.

Contents

List of Figures

Sommario

L'epilessia è un disordine cerebrale caratterizzato dalla predisposizione alle generazione di attacchi convulsivi dovuti ad una attività cerebrale eccessiva o sincrona, provocando cambiamenti nell'attenzione e nel comportamento del paziente. Una volta classificata, la malattia è solitamente trattata con farmaci anti-epilettici. Tuttavia, tra il 20% e il 40% dei pazienti che soffrono di epilessia focale sono farmaco-resistenti [20]. I pazienti di questa categoria sono possibili candidati per una cura chirurgica, che ha lo scopo di rimuovere la zona epilettogena (EZ) responsabile delle crisi.

Metodi non invasivi, come la video-EEG ed altre indagini neuro-radiologiche, aiutano a localizzare la EZ in fase di pianificazione chirurgica pre-operatoria. Tuttavia, la EZ può non essere identificata con metodi non invasivi in circa il 25% dei pazienti, rendendo necessaria un analisi tramite elettroencefalografia (EEG) intracranica [12].

La stereo-EEG (SEEG) è una tecnica mini-invasiva guidata da immagini per la localizzazione della EZ. Si basa sull'impianto percutaneo di molti elettrodi intracerebrali per l'ispezione di strutture cerbrali sia superficiali che profonde.
In una procedura SEEG, le traiettorie d'impianto degli elettrodi richiedono una pianificazione complessa che richiede molto tempo. Inoltre, devono essere presi in considerazione diversi vincoli: l'assenza di vasi sanguigni nell'area di ingresso (EP) dell'elettrodo, devono essere evitati i solchi e prevenire l'incrocio delle traiettorie.

Gli algoritmi di pianificazione computerizzati riducono i rischi derivati dall'impianto degli elettrodi e riducono i tempi computazionali tenendo conto delle restrizioni sopra descritte. Uno dei vincoli più importanti è la distanza tra gli elettrodi e i vasi sanguigni, che deve essere massimizata per ridurre al minimo i rischi di emorragia. Il software considera questa restrizione analizzando le segmentazioni vascolari di immagini come Cone Beam Computed Tomography - Digital Subtracted Angiography (CBCT-DSA) o

Contrast Enhanced - Magnetic Resonance Angiography (e.g. CE-MRA con Gadolinio). L'identificazione manuale della vascolatura cerebrale richiede molto tempo ed è dipendente dal chirugo e, nonché, dalla sua esperienza. L'implementazione di algoritmi automatici o semi-automatici sono una soluzione per ottenere una segmentazione vascolare più accurata e riproducibile e in meno tempo. L'attuale metodo di segmentazione si basa sul thresholding manuale: è una tecnica molto rapida, ma è molto soggettiva e può portare a problemi di pianificazione, soprattutto in caso di dataset rumorosi.

L'obiettivo di questo lavoro è l'estensione dei metodi di segmentazione descritti in [10] per la segmentazione 3D, in modo da essere applicata ad immagini CBCT-DSA ed essere poi inclusa nel software di pianificazione descritto in [36]. In particolare, si è focalizzato sull'implementazione di diversi algoritmi di segmentazione automatica già presenti in letteratura e sulla loro validazione per l'applicazione nel planner SEEG. Infine, il metodo migliore è stato inserito nel workflow del planner automatico.

Per migliorare la segmentazione, sono stati implementati 3 diverse tecniche automatiche di classificazione basate sul modello a gaussiane miste:

- Modello a gaussiane miste semplice (GMM)

- GMM con Markov Random Field (GMM-MRF)

- GMM-MRF basata su Maximum Intensity Projections (MIPs) iterative

Per valutare l'efficacia degli algoritmi di segmentazione implementati, sono stati fatti due esperimenti:

1. Tuning dei parametri: entrambi i metodi GMM e GMM-MRF necessitano di un'inizializione dei corrispondenti parametri, i quali sono stati calibrati per ottenere i risultati migliori per ogni metodo di segmentazione.

2. Confronto degli algoritmi: i metodi di segmentazione sviluppati sono stati comparati in modo da definire quale conduca ad una segmentazione vascolare migliore. Sono stati inoltre confrontati con l'attuale metodo di thresholding manuale.

Gli esperimenti sono stati fatti su un dataset composto da volumi CBCT-DSA di 6 diversi pazienti comparati con un dataset di riferimento composto da 4 diversi sottovolumi per ogni paziente manualmente segmentati da un esperto chirurgo. Gli indici

2

di misura valutati sono: Sensitività, Specificità, Precisione, Accuratezza e l'indice Dice (DSC).

Riguardo la calibrazione dei parametri, entrambi i metodi dimostrano alti valori di Sensitività ed Accuratezza con 3 cluster e un log-likelihood threshold settato a 10; per il GMM-MRF, i parametri beta e neighbourhood mostrano risultati simili per tutti gli indici, quindi sono stati considerati rispettivamente beta = 1.5 e neighbourhood = 26 voxels. Il threshold per la binarizzazione delle immagini è stato settato rispettivamente sul cluster 2 per il GMM e sul cluster 1 per il GMM-MRF. Confrontando gli algoritmi con le combinazioni di parametri così calibrate, si evince che il GMM-MRF ha indici di Sensitività (0.90) e DSC (0.80) più alti rispetto agli altri metodi di segmentazione; questi indici sono importanti in quanto dimostrano quanto il metodo sia in grado di identificare i vasi sanguigni. Inoltre, il GMM-MRF ha mostrato qualitativamente performance migliori rispetto sia al thresholding che il GMM, riproducendo la naturale connessione dei vasi sanguigni anche in presenza di rumore, portando ad una corretta classificazione di vasi sia di grosso che piccolo calibro.

Summary

Epilepsy is a brain disorder characterized by an enduring predisposition to generate epileptic seizures due to abnormal excessive or synchronous neuronal activity, thus causing changes in attention or behaviour. Once the seizure is classified, the disease is usually treated with anti-epileptic drugs. However, between 20% and 40% of focal epilepsy patients are refractory to antiepileptic medications[20]. Such patients are possible candidates for curative surgery, which aims to resect the epileptogenic zone (EZ) that generates seizures.

To plan the surgery, pre-operative non-invasive methods, such as video-EEG and neuro-radiological investigations, help to localize the EZ. However, in about 25% of surgical candidates, the EZ cannot be inferred from non-invasive imaging data, and intracranial electroencephalography (EEG) is needed to identify the EZ[12].

The Stereo-ElectroEncephaloGraphy (SEEG) is a minimally invasive image-guided surgical procedure used to localize the EZ. It relies on percutaneous implantation of numerous intracerebral electrodes surveying superficial and deep structures. In SEEG procedure the electrodes trajectory planning is very challenging and time consuming. Various constraints have to be taken into account simultaneously: the absence of vessels at the electrode Entry Point (EP), sulci avoidance and prevent the crossing between two or more trajectories.

Computer-assisted planning algorithms can reduce implantation risk and time by computing the trajectories taking into account the previously described constraints. One of the most important constraint is the distance between electrodes and brain vessels that has to be maximized to reduce any risk of damage. This is taken into account by the planner algorithm that analyzes the vessel segmentation of biomedical images of the patient such as Cone Beam Computed Tomography - Digital Subtracted

Angiography (CBCT-DSA) or Contrast Enhanced-Magnetic Resonance Angiography (e.g. CE-MRA with Gadolinium). Manual vessels identification is time consuming, subjective and needs experienced surgeons. A solution to this problem is the implementation of automatic or semi-automatic algorithms to perform a more accurate and reproducible vessel segmentation in less time. The actual segmentation method is based on manual thresholding; it is a very fast but user-dependant technique that leads to planification problems, especially in case of noised dataset.

The aim of this work is the extension of the vessel segmentation method described in [10] for 3D volumetric segmentation, to be applied to CBCT DSA images and included in the planning workflow described in [36]. In particular, we focused on the implementation of different segmentation algorithms presented in literature and on their validation for the SEEG planner. The best method was then added in the planner workflow.

In order to optimize the segmentation, three different automatic clustering techniques based on Gaussian mixture model has been implemented:

- Simple Gaussian mixture model (GMM)

- GMM with Markov Random Field (GMM-MRF)

- GMM-MRF based on Maximum Intensity Projections (MIPs)

In order to evaluate the effectiveness of the implemented segmentation algorithms, two different experiments were done:

1. Parameters tuning: the GMM and GMM-MRF need a set of initialization parameters that have been tuned to achieve the best results for each segmentation method.

2. Algorithms comparison: the developed segmentation methods has been compared to identify which technique leads to the best vessel segmentation. The algorithms were also compared with the manual thresholding.

The experiments were done on a dataset composed by CBCT-DSA volumes from 6 different patients and a ground truth dataset composed by 4 different subvolumes

from each patient manually segmented by an expert surgeon. Five indices were used: Sensitivity, Specificity, Precision, Accuracy and Dice similarity coefficient (DSC).

With respect to the parameter tuning, both the methods have higher Sensitivity and Accuracy with 3 clusters and a log-likelihood threshold set to 10; for GMM-MRF the beta and neighbourhood value show similar results for all the indices, thus it was set a medium value of beta=1.5 and a neighbourhood of 26 voxels. The binarization thresholds were set on the cluster 2 and the cluster 1, respectively for the GMM and GMM-MRF methods.

Referring to the algorithm comparison, the GMM-MRF shows higher Sensitivity (0.90) and DSC (0.80) with respect all the other segmentation methods; it is very important because these indices show how good the algorithm is at detecting a vessel and are a measures of unique correspondence. GMM-MRF qualitatively showed better performance over manual thresholding and GMM in reproducing the connected nature of brain vessels also in presence of noise, thus leading to a correct classification of vessel of both small and big caliber.

Chapter 1

Introduction

Epileptic seizures are among the most common neurologic symptoms in all human populations and there are descriptions of seizure types date back at least to the time of Hippocrates. The International League Against Epilepsy (ILAE) conceptually defined epilepsy in 2005 as a "*disorder of the brain characterized by an enduring predisposition to generate epileptic seizures and by the neurobiologic, cognitive, psychological, and social consequences of this condition*" (an epileptic seizure is a transient occurrence of signs and/or symptoms due to abnormal excessive or synchronous neuronal activity in the brain)[35][13].

The Paroxysmal Depolarization Shift (PDS) is the pathophysiological cellular phenomenon that underlies all types of epileptic seizures and interictal epileptiform electroencephalography (EEG) abnormalities ("spikes")[17][24]. As shown in Figure 1.1, PDSs are cellular events in which rapidly repetitive action potentials are not followed by the usual refractory period, thereby generating a prolonged membrane depolarization (which is more prolonged than typically occurs in response to normal excitatory postsynaptic potentials [EPSPs]). An interictal spike is caused by PDSs in large numbers of neurons that are synchronized such that each involved neuron generates one PDS at the same time. An electroclinical seizure occurs when large numbers of neurons in one or more brain regions are repeatedly generating PDSs, in sustained repetitive firing with synchronization.
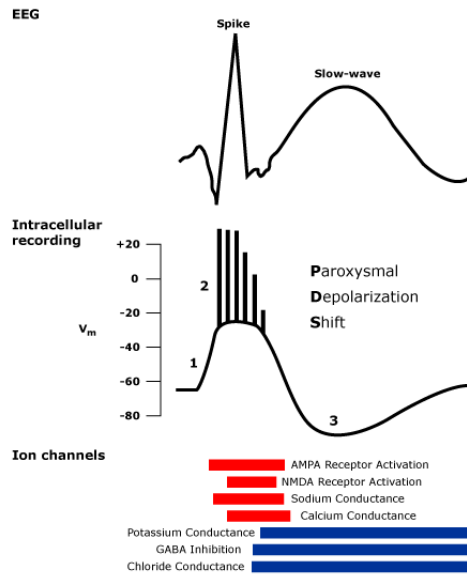
Figure 1.1: The Paroxysmal Depolarization Shift. The prolonged depolarization results in action potentials and propagation of electrical discharges to other cells. The PDS is largely dependent on glutamate excitation and activation of voltage-gated calcium and sodium channels. An electroencephalogram (EEG) recorded during this time would show a spike and a subsequent slow wave. When the balance of excitation and inhibition is further disturbed, there will be a breakdown in containment of the epileptic focus and a seizure will occur.

The first step to diagnose epilepsy is to classify the seizure type. The last operational classification of seizure types proposed by ILAE in 2017 [13](Figure 1.2) defines three major groups based on the location of the epileptic discharges in the cerebral cortex and the extent and pattern of the propagation of the epileptic discharge in the brain:

- *Focal onset*: the origin of the epileptic discharge is limited to one hemisphere. It may be discretely localized or more widely distributed. Therefore, focal seizures have features that allow to identify the involved area.

- *Generalized onset*: it may originate at some point within bilaterally distributed networks. Such bilateral networks can include both cortical and subcortical structures, therefore, individual seizure onsets can appear localized. Generalized seizures can be asymmetrical, thus causing the distinction from focal onsets harder.

- *Unknown onset*: seizures are broadly categorized as either generalized or focal, but there are some cases that cannot be categorized in this manner.
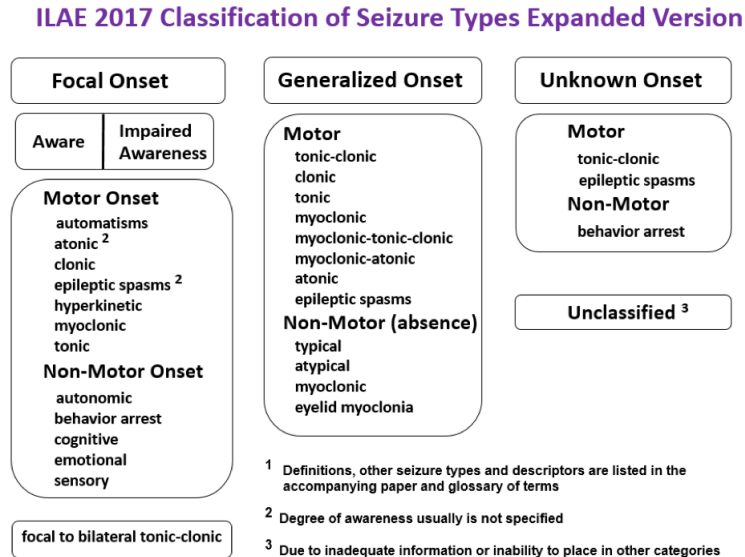
Figure 1.2: ILAE 2017 seizure classification[13].

Once the seizure is classified, the disease is treated with anti-epileptic drugs. However, between 20% and 40% of focal epilepsy patients are refractory to antiepileptic medications[20]. Such patients are candidates for curative surgery, which aims to resect the epileptogenic zone (EZ) that generates seizures. This is an invasive procedure and, before proceeding, it's important to investigate where the EZ is located. Non-invasive methods such as video-EEG, MRI, Flair, PET and neuropsychological tests are used, however, they don't always lead to the desired results and cannot provide definitive information for a good surgery planning[47]. In about 25% of surgical candidates, the EZ cannot be inferred from non-invasive imaging data, and intracranial electroencephalography (EEG) is needed to identify the EZ[12]. Thus, the accuracy in finding the EZ is mandatory to avoid post-operative permanent neurological deficits. One of the invasive procedures for localizing the seizure foci is the intracranial EEG with cortical grid. It requires the placing of a large array of electrodes called a subdural grid on the surface of the brain[31]. To expose the brain's surface, patients need to undergo a larger surgery called craniotomy. This method is invasive, risky and can only record cortical activity. In contrast to intracranial electrode studies with subdural

grid and strip electrodes with sparse depth electrodes for less accessible structures, the Stereo-ElectroEncephaloGraphy (SEEG) is a minimally invasive image-guided surgical procedure used to localize the EZ. It relies on percutaneous implantation of numerous intracerebral electrodes surveying superficial and deep structures. Thus, it requires a more accurate and precise surgery planning because of the large number of implanted electrodes (trajectory planning is the most significant part in order to avoid important brain structures) but it gives information about deeper structures and it reduces the hospitalization time of the patient.

1.1   Stereo-ElectroEncephaloGraphy

The Stereo-Electroencephalography (SEEG) is a minimally invasive surgical practice introduced in the second half of the twentieth century by Bancaud and Talairach at the S. Anne Hospital, Paris, France. In Italy however it was introduced by Munari et al. in the mid-1990s[29].

It consists in implanting intracranial electrodes in the brain through small openings in the skull (Figure 1.3) when the non-invasive data are insufficient to define the epileptogenic zone (EZ).
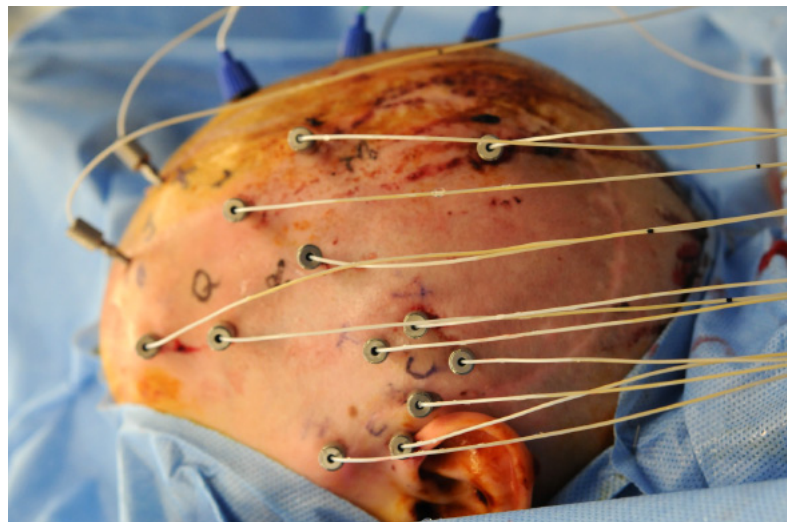

Figure 1.3: Example of SEEG electrodes. This example show the high number of electrodes necessary for SEEG and the importance of their distribution.

Sophisticated software and imaging technology are needed to monitor the placement of the intracranial electrodes, and only a handful of institutions like Niguarda Ca' Granda Hospital in Milan uses this approach.

In recent years, thanks to the advances in robotic surgery and biomedical imaging, there have been many improvements in SEEG procedure, both for the accuracy and for the safety of the patients[7][29].

The electrodes can precisely record the electrical activity of brain structures, detecting patterns of electrical abnormalities that can define the seizure foci, or find the functional cortical areas which are responsible for seizures. This technique avoids open surgery, and many argue that it provides superior coverage of medial and deep structures, as well as certain common epileptogenic networks[6].

The minimally invasive nature of SEEG makes it safer [4][7][41] and patients are likely to have less pain and better wound healing. Candidates for this methodology are determined by radiological investigations, type of seizures, and other patient-specific factors.

SEEG procedure can be divided into four major blocks(Figure 1.4):

1. *Images fusion*: all the biomedical images acquired are properly treated and merged to obtain a brain image as clear as possible.

2. *Planning electrodes trajectories*: surgeons, using the available images, plan electrodes trajectories respecting various constraints (avoid blood vessels, sulci and trajectories crossing).

3. *Intracranial electrodes placement*: electrodes are placed following the trajectories previously planned.

4. *Signal record and analysis*: the EEG captured from the electrodes is analysed to localize the EZ.
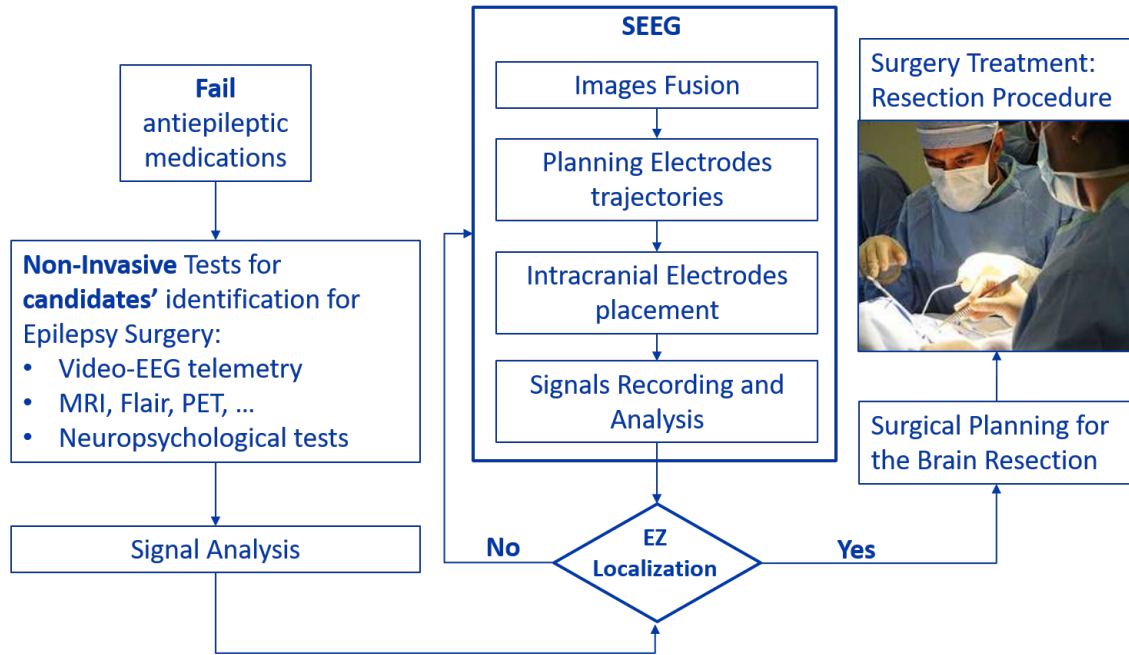
Figure 1.4: SEEG typical workflow. Multiple failures of the anti-epileptic drug treatment and the impossibility of identifying the EZ with non-invasive procedures lead to the application of the SEEG procedure to recognize the epileptogenic area to be resected. This scheme highlights the four main steps of the SEEG: image fusion, electrodes trajectory planning, electrodes placement and signal recording and analysis.

Image fusion

The acquired biomedical images are co-registered and merged in order to be used by the team of neurosurgeons and neurologists to do a first image analysis. The different acquisitions enhance the most important structures to be identified (such as vessels or brain sulci) and the co-registration with intra-operative images allow the surgical navigation with Computed Aided Systems (CAS) during the surgery. The EEG recording can be also co-registered and synchronized with a video source that registers the behaviour of the patient during the entire SEEG procedure (only important parts of the video, such as the scenes correspondent to the seizure events, are stored).

Planning

Intracranial electrode placement step is very delicate during the SEEG procedure because a small error in the calculation of a trajectory may cause serious harm to the

12

patient. Thus, the pre-operative planning of the electrodes trajectories is the most important part of the SEEG procedure.

Preoperative planning of electrodes trajectories reduces implantation risk by ensuring the avoidance of dangerous structures (e.g. arteries, veins, sulci) and conflicts between electrodes.

The safe implantation of intracerebral electrodes for SEEG critically depends on accurate surgical planning and stereotactic technique, with an incidence rate of hemorrhage under 0.2% per electrode and 3% per patient[16][7]. Several skull holes ($\sim 2.1mm$ in diameter) are percutaneously drilled and, due to the dense vasculature of some targets such as the operculo-insular region, many centers make use of angiography datasets in the planning procedure[27]. SEEG planning is traditionally based on the stereotaxic angiographic study of the vascular anatomy[18]. In recent years, researches on electrode trajectory planning to assist clinicians are becoming largely spread[10][38]. This procedure can be used to select the best trajectory (automated planning) or inform manual trajectory selection (assisted planning).

The planning of the stereotactic trajectories is performed by a neurosurgeon, following the results of a multidisciplinary meeting with the epileptologists, who manually selects the target and the entry points (TP and EP respectively)[7] by visually inspecting multimodal anatomical and functional 3D images. The 3D images commonly used for the pre-operative planning are Magnetic Resonance Images (MRI), 3D rotational angiographies and Cone-Beam Computed Tomographies (CBCT)[10][46]. As stated in the previous paragraph, such kind of images allow to enhance critical structures, such as vessels and important brain areas, to be avoided in order to reduce the implantation risks.

To enable a faster planning process and ensure safety of the resulting implantation plan, the correct positioning of intracerebral electrodes must address some essential requirements:

- Critical structures have to be clearly identifiable;

- All of the trajectories must not intersect any critical tissue (e.g. vessels and sulci) to avoid harm to the patient;

- Minimizing the risk of complications such as intracranial bleeding, infections and cerebrospinal fluid leakage;

- Accurate targeting of desired intracerebral structures;

- The trajectories should be further from any critical tissue by a specified safety distance: this margin is based on the wanted accuracy of the surgical procedure of electrodes implantation;

- The trajectory should be as short as possible;

- The entry angle of the trajectories should be as close to 90 degrees as possible: to allow robust implementation of the planned entry angle during the surgical procedure.

Usually, up to 20 electrode shafts are planned, making the manual planning a hard and time consuming procedure.

Computer-assisted planning algorithms can reduce implantation risk and time by computing the trajectories taking into account the previously described constraints. One of the most important constraint is the distance between electrodes and brain vessels. The recommended minimum distance between the entry point and the nearest vessel is $3 - 4mm$ to ensure the absence of complications during the implantation phase for the patient. In deeper brain regions the distance between electrode and vessels could become even smaller (up to $1mm$)[27].
Manual vessels identification is time consuming, subjective and needs experienced surgeons. A solution to this problem is the implementation of automatic or semi-automatic algorithms to perform a more accurate and reproducible vessel segmentation in less time.

This is taken into account by the planner algorithm that analyzes the vessel segmentation of biomedical images of the patient such as CBCT-DSA (Cone Beam Computed Tomography - Digital Subtracted Angiography) or Contrast Enhanced-MRA (e.g. CE-MRA with Gadolinium). There are several algorithms to segment images but the precision and the accuracy in brain vessel segmentation is still a problem.

14

Electrodes placement

To surgically place the electrodes following the planned trajectories, it is necessary to fix the head of the patient and register its position with the images used in the pre-operative planning. Electrodes can then be surgically positioned by using frameless or frame-based stereotactic techniques or a robotic assistant, such as Neuromate® (Renishaw Mayfield, Nyon, Switzerland) or ROSA® (Medtech, Montpellier, France), which automatically aligns the tool holder along the planned trajectories[9].

Signal record and analysis

Each single electrode is tested before the recording of the signal in order to reduce the risk of SEEG failure. Then, the patient is asked to perform specific tasks (e.g. reaching tasks, visual stimuli, ...) so that the neurologist, based on these trials, decides the contacts that have to be recorded and displayed. After these trials the patient undergoes to electrical stimuli such as electric pulses, to evaluate brain's areas activation, or electrical train of pulses (to provoke an epileptic seizure and to identify the EZ). The recorded responses to the stimuli are recorded (Figure 1.5) and further analyzed by the neurologist.
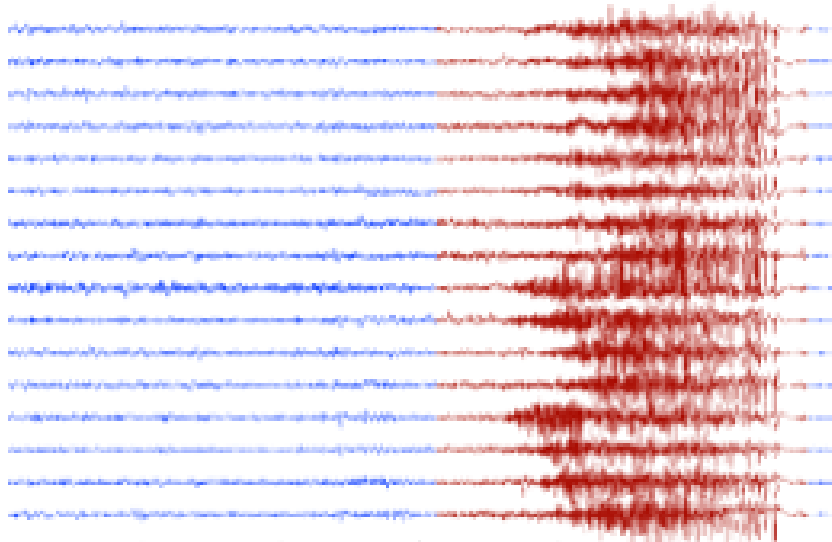

Figure 1.5: Example of a SEEG record.

All the informations from the SEEG, the acquired biomedical images and the patient's clinical and family history are merged in order to be analyzed and to define the possibility of the EZ resection. Thus, when it is possible the brain area resection proposal is discussed with the neurosurgeon.

Chapter 2

State of the art

As introduced in chapter 1 medical images have a foundamental role in various medical fields, especially in early disease diagnostic and for pre-operative planning. Analysis of medical images first requires the identification of the regions of interest (ROIs). *Image segmentation* is the procedure to extract ROIs. Accurate visualization and quantification of blood vessels play a significant role in a number of clinical procedures. For various medical diagnostic tasks, it is necessary to measure the vessel width, reflectivity, tortuosity, and abnormal branching. Planning and performing neurosurgical procedures require an exact insight into blood vessels and their branches, which exhibit great variability. In planning, they provide information on where the blood is drawn and drained, to differentiate between the feeding and transgressing vessel. During surgery the vessels serve to provide landmarks and guidelines to the lesion. In short, accuracy in the navigation and localization of clinical procedures is determined by how minute and subtle the vascular information is[11]. In particular, during the pre-operative planning for SEEG procedures, the vessels have to be precisely identified in order to be avoided. In fact, vessels identification is the most important constraint to prevent brain damages and risky situations. In case of automatic planning the vessel segmentation plays a significant role, because it directly and heavily influencies the trajectory planning. Thus, image segmentation is the most important part of the processing of medical images in pre-operative planning of brain surgery applications and requires high accuracy and precision. Manual segmentation is subjective and time-consuming, so it needs improvements to make it faster and operator independent.

The implementation of automatic or semi-automatic processes may lead to better and objective results in less time.

This section describes in details the actual state of the art about segmentation algorithms and, especially, their developments in vascular detection for brain surgery applications.

2.1 Image segmentation

Image segmentation methods relies on the principle of labeling structures with specific characteristics. Thus, the result of a segmentation is usually a binary mask where the enlightened structures are the regions of interest. Image segmentation methods can be divided into two major groups:

- *Edge-based*: edge-based methods are based on discontinuities of ROIs contours. The final segmented structure is described by the separation contour/surface from the rest of the image.

- *Region-based*: these methods are based on homogeneity of the regions of interest. Intensity of voxels is the main characteristic considered for region-based algorithms. The final segmented structure is described as an occupied region.

2.1.1 Edge-based segmentation methods

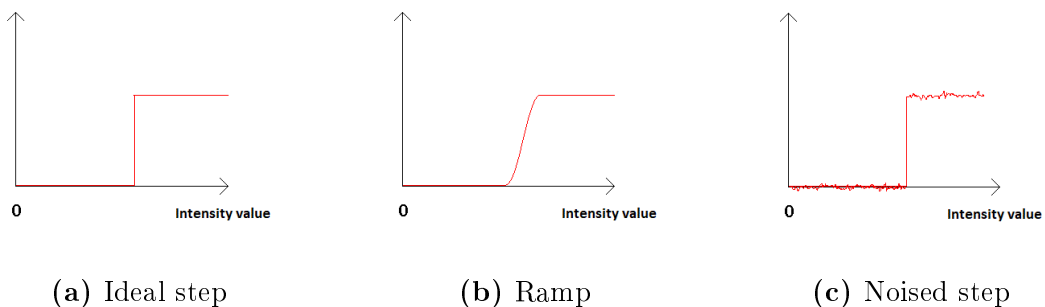(a) Ideal step   (b) Ramp   (c) Noised step

Figure 2.1: Possible typologies of edges

Edge-based segmentation techniques relies on the principle of abrupt intensity changes in correspondence of the edges and contours of the objects (Figure 2.1). In reality the

intensity difference along boundaries are not so rapid because of the noise.

Derivative operators

This approach is based on the searching for discontinuity using derivative operators. The first order derivative operator is the gradient operator (Δf):

$$\Delta f = [G_x, G_y, G_z]^{-1} = \left[\frac{\partial f}{\partial x}, \frac{\partial f}{\partial y}, \frac{\partial f}{\partial z}\right]^{-1} \tag{2.1}$$

The second order derivative operator is the Laplacian:

$$\nabla^2 f(x, y, z) = \frac{\partial^2 f}{\partial x^2} + \frac{\partial^2 f}{\partial y^2} + \frac{\partial^2 f}{\partial z^2} \tag{2.2}$$

It is not commonly used by itself as edge detector, as it is very sensitive to noise. Moreover, it results in a double contour (Figure 2.2) and it is not able to indicate the edge direction. However, it is utilized together with other edge detectors, to localize potential edges.
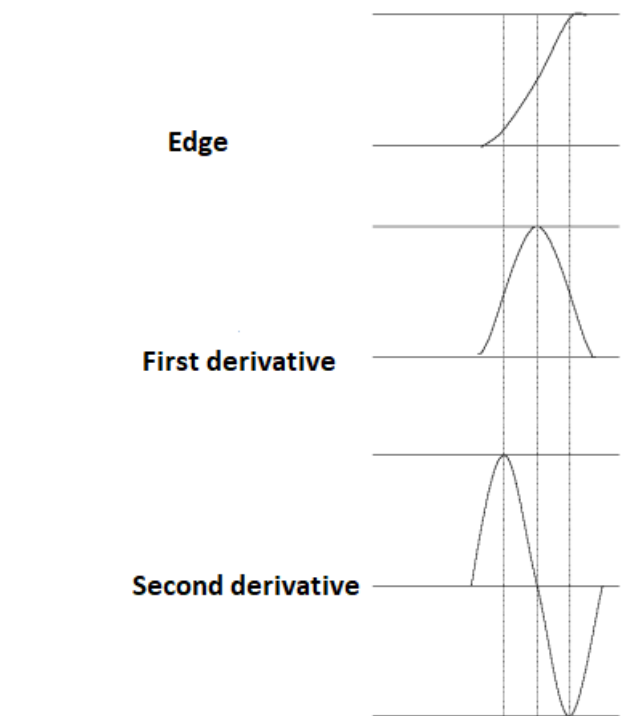

Figure 2.2: This figure represents the first and the second order derivative operator applied on edges.

The image is a discrete function with two variables which we can approximate to the sum of conveniently delayed and weighted impulses.

$$I_{(m,n)} = \sum_i \sum_j I_{(i,j)} \delta_{(m-i)} \delta_{(m-j)} \tag{2.3}$$

The derivative operation equals to the convolution between the image $I(M \times N)$ and a kernel $K(m \times n)$, being this latter defined to be sensitive to the intensity variations:

$$O_{(i,j)} = \sum_{k=1}^{m} \sum_{l=1}^{n} I_{(i+k-1,j+l-1)} \cdot K_{k,l} \tag{2.4}$$

with $i = 1 \ldots M - m + 1$ and $j = 1 \ldots N - n + 1$.

Derivative operation is very sensitive to noise, thus it needs to combine a smoothing procedure. Examples of gradient operator kernels are shown in figure 2.3.
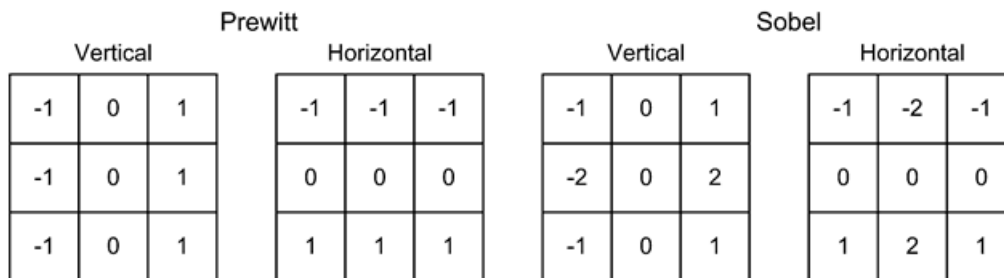
Figure 2.3: Prewitt and Sobel gradient operator kernel are used to estimate the gradient of the image intensity at each point of a 2D image.

Dynamic programming

Dynamic programming is an edge-based segmentation method that works with deformable contours (*snakes*) or surfaces (*balloon*). Conceptually, the dynamic contour attempts to shrink a boundary to image features. The algorithm's major advantage is that it is able to bridge discontinuities in the image feature being located[19]. First, the contour is manually initialized, then it is attracted by edges in the 2D image and deformed accounting for specific mechanical features initially attributed to the contour. The contour is shrunk with length and stiffness constraints; shrinking is opposed by constraints derived from the image data which are dependent on the type of boundary being located. For example, if a local maximum was being traced, the constraint could

be derived as a weighted sum of the local gray values; if a contour was being followed, the constraint would be derived from the image gradient. The algorithm allows the relative influences of these three factors (length, stiffness, image feature) to be varied and thus allows the user to tune the snake to a particular shape of boundary[28].

The snake algorithm works on a cost function interpreting the internal (*elastic*) energy of the contour and on the presence of attracting elements (discontinuities, edges):

$$E^*_{snake} = \int_a^b (E_{int}[v_{(s)}] + E_{ext}[v_{(s)}])ds \tag{2.5}$$

with E_{int} interpreting the elasticity of the contour and E_{ext} which interprets the attraction energy exherted by edges.

The desired contour is then defined by the minization of the cost function:

$$B^*_N = \{B_N \mid min(E_{B_N})\} \tag{2.6}$$

Isosurfacing methods

Isosurfacing techniques looks for homogeneity 3D. The algorithms are directly applied to the gray-level volume and they combine segmentation with boundary surfaces generation and their representation. There are two principal techniques:

- *Cuberille model*: it requires an initial gray-level volume binarization (so, a specific threshold is defined) or a criteria to classify voxels as belonging or not belonging to a specific structure.

- *Marching cubes*: it requires the initial definition af a threshold for voxel classification and exploits intensity for boundary data.

Cuberille model   The Cuberille model search for surface of separation between voxels previously binarized[33]. This method consider each voxel v_i as a cube, so that the surface of separation between the voxel v_i and its neighbours is defined by their binary classification.
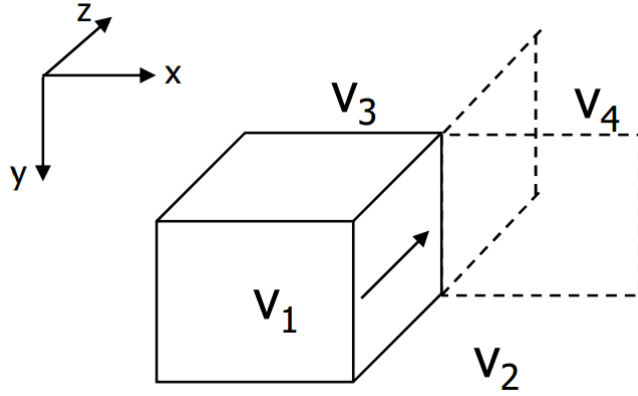
Figure 2.4: Example of Cuberille model application with four voxels.

As in Figure 2.4, the separating voxel surface is identified as the voxel face between a voxel below threshold and one of its neighbours above the threshold:

$$g(v_1) \geq T \ \& \ g(v_2) < T \tag{2.7}$$

with $g(v_1)$ and $g(v_2)$ are the intensities of the voxel 1 and voxel 2 respectively. The other separating voxel faces are identified according to the intensity values of the surrounding voxels:

$$v_2 - v_4 \qquad \text{if } g(v_3) \geq T \ \& \ g(v_4) \geq T \tag{2.8}$$

$$v_1 - v_3 \qquad \text{if } g(v_3) < T \ \& \ g(v_4) \geq T \tag{2.9}$$

$$v_3 - v_4 \qquad \text{in other cases (for continuity)} \tag{2.10}$$

Marching Cubes This method consider eight voxels as the vertices of a voxel cube (Figure 2.5) and their intensity level are assessed as a function of the predefined threshold T[23].
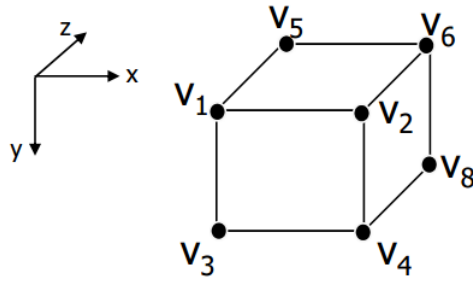
Figure 2.5: Marching cubes. The marching cubes technique consider eight neighbouring voxels as the vertices of a voxel cube.

Let v_1 the voxel that belongs to the considered object:

$$g(v_1) \geq T \text{ \& } g(v_i) < T \qquad \text{(with i=2,3,\ldots,8)} \qquad (2.11)$$
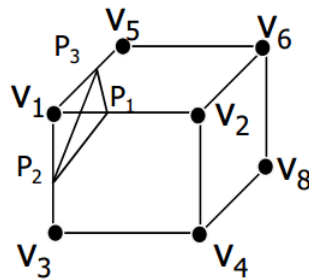
Figure 2.6: The separating surface is defined by the points that represent the points along the lines connecting above versus below threshold voxels at which the intensity level equals the predifened threshold T by means of linear interpolation.

Along the lines connecting the above-threshold versus below-threshold voxels, the points at which the intensity level equals the predefined threshold T by means of linear interpolation are considere. The identified points are the vertex of a surface element which will define the separating surface. There could be 256 possible cases, but they are reduced to 15 because of simmetry. However there are ambiguities as shown in Figure 2.7.

23

Figure 2.7: Example of an ambiguity with marching cubes.

To resolve the ambiguities manual refinement or an analytical resolver are needed. The marching cubes technique requires optimization and has high computional cost.

2.1.2   Region-based segmentation methods

As introduced in the previous paragraph region-based algorithms are based on homogeneities of the image, so these methods recognize ROIs with similar characteristics (e.g. intensities, colors, textures, ecc).
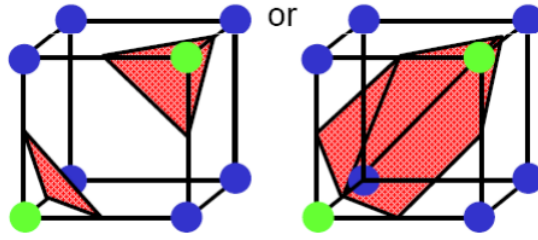
Threshold-based techniques

Global thresholding method is the easiest but practical and efficient approach for vascular segmentation. As vessels are enhanced by the use of a contrast agent or others imaging techniques, global threshold is good enough for several clinical applications. It is based on the assumption that specific ROIs have a specific range of intensities. Thus, the separation of the objective pixels/voxels from the background is accomplished by the selection of a gray-level θ. This is a process that classifies pixels/voxels as under/over threshold (*binarization*) so that:

$$g(x,y) = \begin{cases} 1, & \text{if f(x, y)} \geq \theta \\ 0, & \text{otherwise} \end{cases} \tag{2.12}$$

where f(x, y) is the intensity value of the pixel (x, y).

Threshold selection is crucial, especially for important structures such as vessels. Threshold can be selected in many different ways:

- *Trial error*: it is chosen after several trials to fit the best result. It is a trivial

24

and subjective way to select it for vascular segmentation, but could be an initial step to find out the gross intensity interval where it leads to nice results.

- *Function of gray level histogram*: the gray level histogram is a key-point in threshold selection; it can be unimodal (binarization) or multimodal (clustering).

- *Variable threshold on different image regions*: the image is subdivided in different regions and each region has a specific threshold.

- *Band/bi-level thresholding*: the threshold is set as an interval of interest, so it is bounded between two values;

$$g(x,y) = \begin{cases} 1, & \text{if f(x, y)} \in D \\ 0, & \text{otherwise} \end{cases} \tag{2.13}$$

with D a specific gray level interval.

The threshold selection as a function of gray level histogram requires the analysis of frequencies distribution. In case of multimodal histogram (as shown in Figure 2.8), thresholds are usually selected in correspondence of minima between local adjacent maxima.
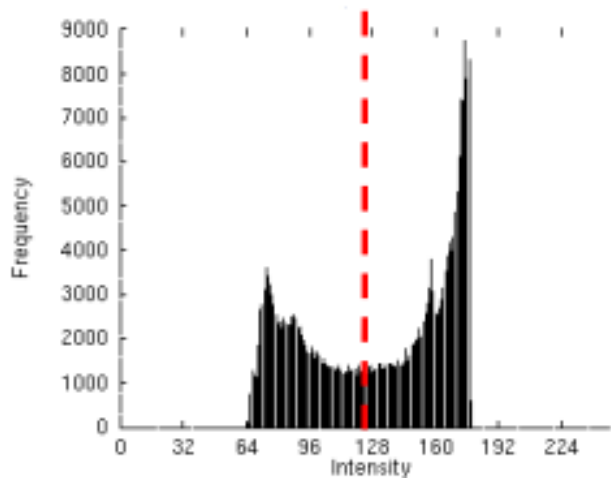

Figure 2.8: Example of threshold selection in case of bimodal histogram. In this example the histogram shows two high peaks that correspond to two different structures, so the threshold is selected in correspondence of the minumum between the two adjacent maxima.

25

Region growing techniques

Region growing methods are clustering techniques of pixels/voxels with similar features. Homogeneity is the main selection criteria (e.g. homogeneity of gray-levels, colors/texture, ...). In 1994 Adams and Bischof proposed the so called Seeded Region Growing (SRG) algorithm. It is fast, robust and parameter free. As the name suggests, it needs a set A of n seeds (individual points or connected components) as inputs. The seeds play the same role as the markers used in watershed segmentation[26]. Let T be the set of all unallocated pixels/voxels that border at least one of the A:

$$T = x \notin A : N(x) \cap A \neq \varnothing \tag{2.14}$$

where $N(x)$ represents the set of immediate neighbours (6, 18 or 26) of the pixel/voxel x. A single step of the algorithm involves examining the neighbours of each $x \in T$ in turn[2]. For each element the similarity measure $\delta_{(x)}$ between x and the intersected region is calculated as:

$$\delta_{(x)} = \mid g(x) - mean_{y \in A}\{g(y)\} \mid \tag{2.15}$$

where g(x) is the intensity (gray value) of the pixel x. If $N(x)$ intersects more than one region then A is taken to be that region for which $\delta_{(x)}$ is a minimum. In this way a δ value is determined for each $x \in T$. The pixel $x \in T$ that satisfies

$$\delta_{(z)} = min_{x \in T}\{\delta_{(x)}\} \tag{2.16}$$

is appended to the region corresponding to $\delta_{(z)}$[25]. The process continues until all the pixels/voxels have been connected to the correspondent region.

Clustering techniques

Clustering is a method to divide a set of data into a specific number of groups called clusters. One of the popular method is *k-means clustering*[**macqueen1967**]. K-Means algorithm is an unsupervised clustering algorithm that classifies the input data points into multiple classes based on their inherent distance from each other. It takes as inputs the number of cluster (K), the initial centroids of the clusters and a distance

function $dist(x_i, x_k)$ that expresses the disomogeneity between each pair of input data (x_i, x_k). Let $C_h, h = 1, 2, ..., K$, be a cluster and z_h its centroid:

$$z_{hj} = \frac{\sum_{x_i \in C_h} x_{ij}}{card C_h} \tag{2.17}$$

Afterwards, for each pixel the distance between the current pixel and the center of each cluster is computed. The pixel is then classified according to the distance: it will belong to the cluster with shorter distance. The process is iterative and it will continue until no reassignment is operated or the maximum number of iterations is reached. The K-means algorithm can be summarized in four easy steps:

1. **Initialization**: first it is necessary to initialize the number of cluster and the initial centroids of the clusters (randomly selected among the input data); in addition it needs the definition of the distance function.

2. **Data classification**: iteratively each observation is associated to the cluster that has the nearest centroid, so that minimizes the distance from the observation.

3. **Centroid update**: each time an observation is assigned to a cluster, the centroid of each cluster is updated.

4. **Convergence**: the step 2 and 3 are repeated until the convergence has been reached, so when none of the points has been reallocated with respect to the previous iteration.
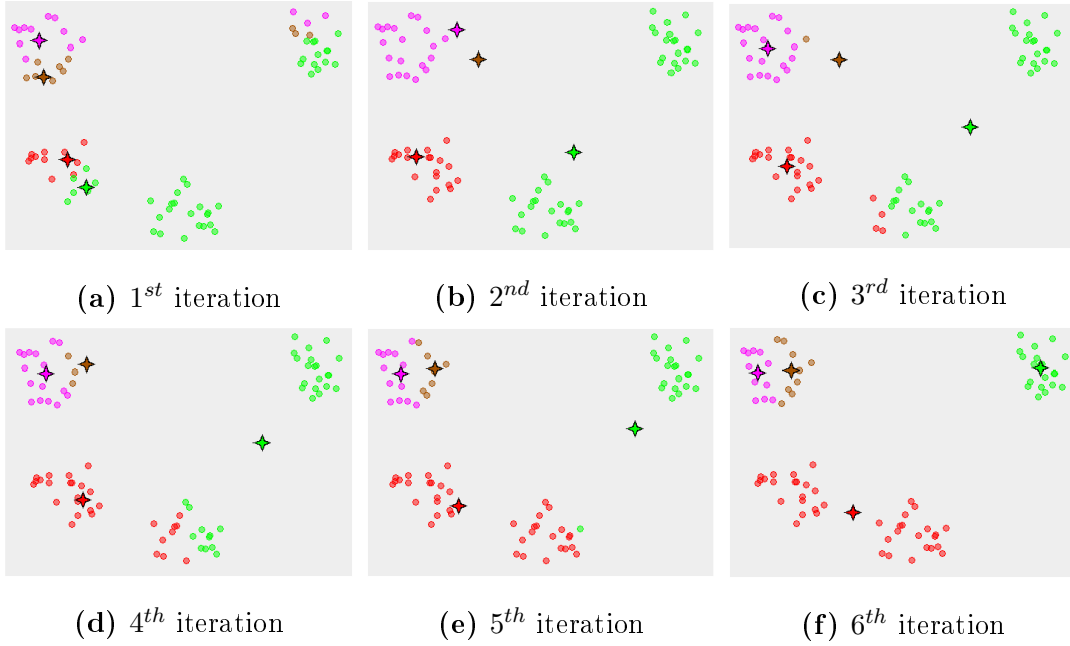
(a) 1st iteration	**(b)** 2nd iteration	**(c)** 3rd iteration
(d) 4th iteration	**(e)** 5th iteration	**(f)** 6th iteration

Figure 2.9: Example of K-means algorithm application.

A more sophisticated clustering technique relies on the Gaussian Mixture Model (GMM). It is a parametric probability density function represented as a weighted sum of Gaussian component densities. Thus, the posterior probability of each observation at the i-th pixel x_i, with $i = 1, 2, ..., N$, belonging to the class Ω_j, with $j = 1, 2, ..., K$, the density function at an observation x_i is given by:

$$p(x_i) = \sum_{j=1}^{K} \pi_j p(x_i | \Omega_j) \tag{2.18}$$

where $p(x_i | \Omega_j)$ is a Gaussian distribution called *component* of the mixture, π_j is the prior distribution of the pixel x_i that belongs to the class Ω_j and satisfies the constraint:

$$\sum_{j=1}^{K} \pi_j = 1 \tag{2.19}$$

It is commonly used as a parametric model of the probability distribution of continuous measurements or features in several applications such as biometric systems (e.g. vocal-tract related spectral features in a speaker recognition system) or image segmentation. GMM parameters are estimated from training data using the iterative Expectation-Maximization (EM) algorithm or Maximum A Posteriori (MAP) estimation from a well-trained prior model[32]. The complete Gaussian mixture model is

parameterized by the mean vectors, covariance matrices and mixture weights from all component densities.

R. Gan et al. in [15] propose an automatic statistical vascular segmentation on three-dimensional rotational angiography (3D-RA). The implemented iterative approach to segment the 3D vascular structure is based on segmentations of MIP images across iterations and then followed by a refinement technique. Each one of the classification groups are estimated with the GMM with Markov Random Field (MRF) modification to estimate the a-priori probability based on neighbouring pixels/voxels. This method takes advantage of the MIP as it decreases the standard deviation of each class. A detailed explanation of this segmentation method is presented in the next section.

2.2 Vessel segmentation techniques

The segmentation techniques exposed in section 2.1 are general methods for image segmentation but vessel segmentation needs more vessel-oriented approaches in order to identify the vascular tree in the most precise way.

A group of techniques that performs vessel segmentation, independently from the analyzed body district, are the methods that perform vessels enhancement, through filtering, followed by a thresholding step. Different vessels enhancement techniques are presented in literature, and a classification can be done according to the filtering approach designed to enhance the structures of interest.

2.2.1 Matched filtering

Matched filters (MF), which were originally applied in one dimensional signal processing applications [21], are commonly adopted in image processing. MF are designed as to extract features of interest in the image. The filter is therefore convolved with the input image and the output will have higher intensities where those features are present. Two main assumptions are made to extract vessels:

- Vessels are piecewise linear: this assumption follow the hypotesis that vessels are elongated structures with limited bandnig (for healthy vessels).

29

- Vessel cross-section is shaped as a Gaussian with standard deviation (σ) equal to the vessel radius.

Chaudhuri et al. in [8] first introduced vessels segmentation with MFs, where a 2D filter is build to segment retinal vessels. The MF kernel with the orientation angle θ is:

$$K_{MF}(x, y; \theta_n) = \frac{1}{\sqrt{2\pi}\sigma} e^{-\frac{x'^2}{2\sigma^2}} - m \tag{2.20}$$

where m is a constant introduced to normalized the filter mean value to 0 and x' is given by the relation:

$$x' = x\cos(\theta_n) + y\sin(\theta_n) \tag{2.21}$$

It holds the constraint:

$$|-y\sin(\theta_n) + x\cos(\theta_n)| \leq \frac{L}{2} \tag{2.22}$$

where L is the length of the considered linear tract of the vessel. The final binary mask is obtained using an automatic, non-parametric and unsupervised thresholding algorithm that maximizes the separability of the resultant classes basing on the MF output histogram. This approach has been modified by [44] to overcome the MF limit of responding to non-vessel edges because of the strong response of both the vessels and the edges. The first order derivative of Gaussian (FODG) is used because of its low response in correspondence of vessel structures, while it has a high one in correspondence of the edges.

$$K_{MF}(x, y; \theta_n) = \frac{1}{\sqrt{2\pi}\sigma} e^{-\frac{x'^2}{2\sigma^2}} \tag{2.23}$$

2.2.2   Vesselness approaches

Such kind of approaches are inspired by the work of Sato et al. [34] that define a measure of the likelihood for a vessel to be present analyzing the Hessian (H) of the image $I(x, y)$:

$$H = \begin{vmatrix} \frac{\partial^2 I_{(x,y)}}{\partial x^2} & \frac{\partial^2 I_{(x,y)}}{\partial x \partial y} \\ \frac{\partial^2 I_{(x,y)}}{\partial x \partial y} & \frac{\partial^2 I_{(x,y)}}{\partial y^2} \end{vmatrix} \tag{2.24}$$

H is chosen because it describes the second-order structures present in the image as vessels in the analyzed context and, moreover, since it is anisotropic, it describes also

the vessels orientation. The vesselness measure is exctracted from the eigenvalues of the H matrix ($\lambda_1, \lambda_2, \lambda_3$ with $|\lambda_1| \leq |\lambda_2| \leq |\lambda_3|$). The vesselness measure assumes differet values according to the pattern of the structures to be extracted (Figure 2.10).

2D		3D			structure
λ_1	λ_2	λ_1	λ_2	λ_3	
-	-	L	L	H-	bright plane
-	-	L	L	H+	dark plane
L	H-	L	H-	H-	bright tubular
L	H+	L	H+	H+	dark tubular
H-	H-	H-	H-	H-	bright blob
H+	H+	H+	H+	H+	dark blob

**Figure 2.10:** Hessian matrix eigenvalues for different orientation pattern. (H = high value, L = low value)

Considering elongated vessels, λ_1 is significantly smaller than the other eigenvalues. This is why it is associated with the direction of minimum intensity variation (the one parallel to the vessel axis). Furthermore, following the assumption that the intensity of the vessels cross-section is Gaussian-shaped, λ_1 and λ_2 are almost equal because the intensity variation is more or less the same. Image partial second derivatives are computed convolving the image with partial derivative of Gaussian. Then, a multi-scale integration is commonly made to take in account for vessels with different thickness, varying the standard deviation of the Gaussians. Not all the eigenvalues are included in the vesselness measure, thus implies losing meaningful information in the image analysis. Frangi et al. [14] introduce a different vesselness measure that takes in account all the eigenvalues of the H matrix to enhance tubular-like, plate-like and bloblike structures. A measure based on the Frobenius Hessian norm is also introduced in the vesselness computation to distinguish non-informative background from structures of interest.

$$||A||_{Frobenius} = \sqrt{\sum_{i=1}^{n} \lambda_i^2} \tag{2.25}$$

In noisy regions the Frobenius norm is small because the eigenvalues are negligible. Eigenvalues contribution is weighted by three parameters that control the sensitivity of the filter, allowing slightly modify the filter response in relation with the analyzed

context. The analysis is still developed in a scale-space framework. However the Frangi's vesselnes method is not suitable for detecting vessels with complex architectures such as vessel bifurcation. Vesselness-based approaches do not lead to binary masks thus other thresholding or classification techniques have to be adopted.
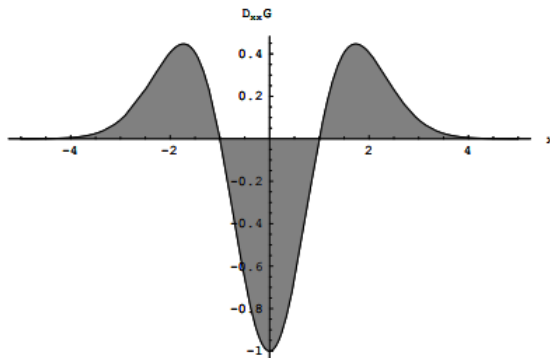
(a)
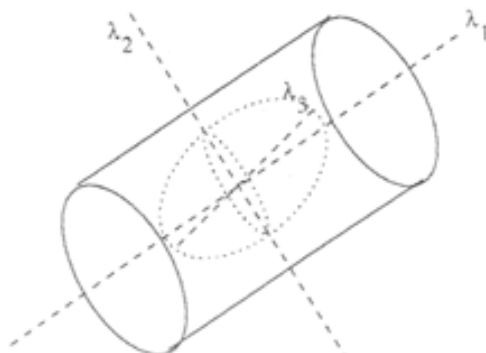
(b)

Figure 2.11: (a): Second order derivative of a Gaussian kernel (inverse Mexican Hat) probes inside/outside contrast of the range $(-\sigma, \sigma)$. In this example $\sigma = 1$. (b): The second order ellipsoid describes the local principal directions of curvature.

2.2.3 Diffusion filtering

Diffusion filtering concept was introduced in [40] and further developed in [25]. The diffusion formulation is:

$$\frac{\partial I(\mathbf{r}, s)}{\partial s} = \nabla(D(I, \mathbf{r})\nabla I(\mathbf{r}, s)) \tag{2.26}$$

where $I(\mathbf{r}, s)$ is the image at coordinate $\mathbf{r}$ and scale s (for scale is intended a scalar related to the degree of resolution in the image, thus bigger is the scale, lower are the details we are able to discriminate and vice versa), and $D(I, \mathbf{r})$ is the diffusion tensor. If D is constant and equal to the identity matrix, the diffusion filtering is equivalent to the linear isotropic Gaussian filtering. In this case, the solution of (2.26), with the original image as initial condition, is a family of images convolved with Gaussians of different standard deviation s:

$$\frac{\partial I(\mathbf{r}, s)}{\partial s} = \nabla^2 I(\mathbf{r}, s) \tag{2.27}$$

with:

$$I(\mathbf{r}, s) = I(\mathbf{r}) \otimes G(\mathbf{r}, \mathbf{s}) \tag{2.28}$$

Thus, the biggest is the standard deviation s, the more blurred is the image.

Weickert et al. [42] in 1997 introduced the edge-enhanced diffusion (EED) and the coherence-enhanced diffusion (CED) filtering techniques. These are two approaches based on anisotropic non-linear diffusion:

$$\frac{\partial I}{\partial t} = \nabla \cdot (D \cdot \nabla I) \tag{2.29}$$

where $\nabla \cdot$ is the divergence operator, ∇I is the gradient of the image and D is the diffusion tensor. The eigenvectors of the diffusion tensor define the principal directions of smoothing and the corresponding eigenvalues define the amount of smoothing. Therefore, the principal directions of smoothing are based on the structure tensor defined as:

$$J_s(\nabla I_\sigma) = K_s * (\nabla I_\sigma \nabla I_\sigma^T) \tag{2.30}$$

where K_s is the Gaussian kernel with standard deviation s and ∇_σ is the gradient of the image I at scale σ. Three-dimensional EED preserves plate-like structures and filters noise from homogeneous areas, while CED filters tubular structures and preserves small spherical structures. Diffusion decreases if the gradient magnitude increases compared to the contrast parameter (λ_e), indicating a plate-like structure. If the gradient magnitude is much smaller than λ_e, isotropic diffusion is performed. Let the eigenvalues of the structure tensor be set in order of decreasing magnitude ($\mu_1 > \mu_2 >$

μ_3). The eigenvalues of the 3-D EED diffusion tensor are defined as:

$$\lambda_{e1} = \begin{cases} 1, & \text{if } |\nabla I_\sigma|^2 = 0 \\ 1 - e^{(|\nabla I_\sigma|^2/\lambda_e^2)^4}, & \text{if } |\nabla I_\sigma|^2 > 0 \end{cases}$$

$$\lambda_{e2} = 1$$

$$\lambda_{e3} = 1 \tag{2.31}$$

with C a threshold parameter set to 3.31488. The eigenvalues of the 3-D CED diffusion tensor are defined as:

$$\lambda_{c1} = \alpha$$

$$\lambda_{c2} = \alpha$$

$$\lambda_{c3} = \begin{cases} 1, & \text{if } \mu_2 = 0 \text{ or } \mu_3 = 0 \\ \alpha + (1 - \alpha)e^{\frac{-\ln(2)\cdot\lambda_c^2}{k}}, & \text{otherwise} \end{cases} \tag{2.32}$$

where $k = (\mu_2/(\alpha + \mu_3))^4$, $\alpha = 0.001$ and λ_c is the CED contrast parameter.

To be able to deal with intermediate geometries of the vessel structures, M. Mendrick et al. [1] in 2009 proposed an hybrid diffusion filter with a continuous switch (HDCS) that combines EED and CED continuously. Thus the eigenvalues of the hybrid diffusion tensor are set to be a linear combination of the eigenvalues of the EED and CED diffusion tensors:

$$\lambda_{h_i} = (1 - \epsilon) \cdot \lambda_{c_i} + \epsilon \cdot \lambda_{e_i} \tag{2.33}$$

where ϵ is the EED fraction that performs the switch between using the eigenvalues of the CED ($\epsilon \to 0$) or the eigenvaluea of the EED ($\epsilon \to 1$) diffusion tensor. As the vesselness-based method, the diffusion filtering based methods do not lead to a binary mask, thus other thresholding or classification techniques have to be adopted.

2.2.4 Deep-learning method

In recent years, the researchers focused their studies on vessel segmentation of 2D and 3D biomedical images with deep learning approaches. In particular, the actual state of the art proposes research on deep learning approaches for fundus oculi images vessel segmentation. Such kind of technique is a class of a broader family of machine learning

algorithms. Neural Networks (NNs) architectures are designed to work with image data, in particular convolutional neural networks (CNNs), and were built already in 1970's (e.g. for pattern recognition). A CNN is a composite of multiple elementary processing units, each featuring several weighted inputs and one output, performing convolution of input signals with weights and transforming the outcome with some form of non-linearity. The units are arranged in rectangular layers (grids), and their locations in a layer correspond to the pixels of the input image (Figure 2.12b).
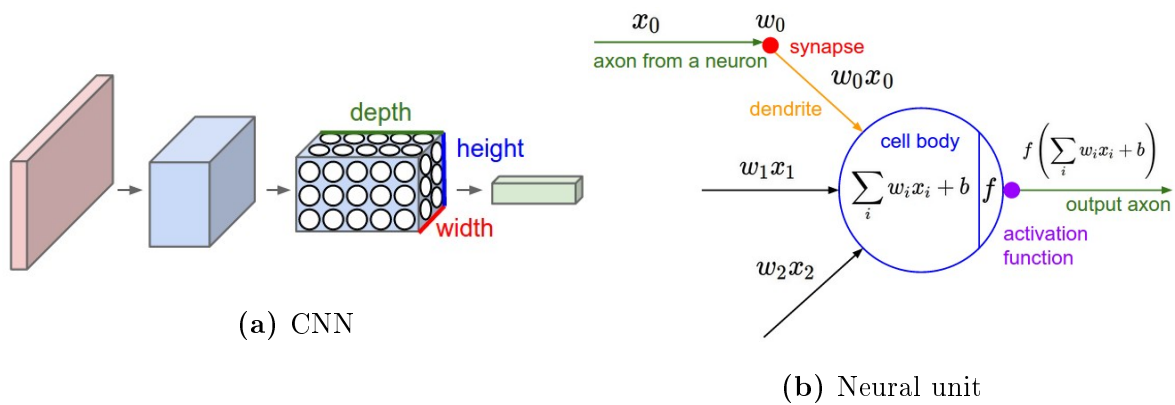

(a) CNN

(b) Neural unit

Figure 2.12: **Left**: A CNN arranges its neurons in three dimensions. Every layer of a CNN transforms the 3D input volume to a 3D output volume of neuron activations. In this example, the red input layer holds the image, so its width and height would be the dimensions of the image, and the depth would be the number of the channels (e.g. 3 in case of RGB channels). **Right**: the neurons of a CNN are simple neurons that fires if the weights combination computed by the activation function overcomes a threshold: they compute a dot product of their weights with the input followed by a non-linearity, but their connectivity is restricted to the RF.(Images from http://cs231n.github.io/convolutional-networks/)

In addition to this characteristic, CNNs have other features:

- *Local Connectivity*: the output of a given unit is proportional to the behaviour of the units inside a Recepteive Field (RF) around it. Local connectivity reduces the number of weights for example in comparison to the fully-connected conventional NNs.

- *Parameter Sharing*: units in the same layer share their weigths, thus forming a feature map and moreover reducing the number of parameters.

- *Pooling*: it consists in aggregating outputs of multiple units by different means with respect to convolution. This is a kind of subsampling, thus reducing the resolution with respect to the previous layer.

In [22] Liskowski et al. proposed a blood vessel segmentation algorithm for retinal images based on a supervised segmentation with deep-learning NN trained on a large dataset. In supervised methods, segmentation algorithms acquire the necessary knowledge by learning from image patches annotated by ground truth. Training consists in an iterative propagation of examples (e.g. images with ground truth) through a NN and the modification of its weights, which are initialized with small signed random values. The backpropagattion of the errors committed by particular units are accumulated and translated into weight updates when a batch (one iteration of the training cycle) is complete. In this paper, they used the error backpropagation algorithm extended with dropout to train the deep-learning NN. This means that with dropout, a subset of network units is drawn at random and temporally 'switched off' during the training. This makes the deep-learning approach more robust and increases its generalization ability.

2.2.5 Vessel segmentation in automated planners for neuro-surgery

As introduced in chapter 1.1, the brain vessels segmentation for automated planner in epilepsy surgery is one of the most important steps because its results have direct impact on the trajectory planning. In literature there are many different segmentation approaches for automated planners. Shamir et al. in [3] and [37] present a preoperative straight trajectory planning method for image-guided keyhole neurosurgery. They use Computed Tompgraphy and Magentic Resonance images to identify risky regions. In particular, for brain vessel segmentation, they use T1 MRI scans. Their approach is based on a vesselness-based enhancement method followed by a skeletonization of the segmented structures; this method is also usually integrated with manual segmentation performed by neurologists in case of misidentification of relevant structures.

In 2014, Zellman et al. [43] proposed an automatic trajectory planning of depth

electrodes for SEEG applications in epilepsy surgery. They used angiographic data (T1-weighted with Gadolinium contrast agent) rescaled to 0.5 mm isotropic resolution and preprocessed with a non local means denoising filter. After the image preprocessing, the vasculature is segmented with Frangi's 3D multi-scale vesselness filter. This filter is sensitive to tubular structures and returns a voxel likelihood of blood vessel presence. As explained in 2.2.2, Frangi 3D filter is an Hessian-based approach. The major drawback of this method is that it tends to underestimate the vessels width, thus, leading to use correction factors during the trajectory planning and causing misidentification of the best trajectories for electrodes placement.

In [45] Zombori et al. used Computed Tomography Angiography (CTA), 3D Phase Contrast MR imaging (3D PC-MRI) and in some cases Time of Flight MRI (ToF MRI) images for extracting the vasculature with a customized tool for SEEG automatic trajectory planner. In [39] they specify that *"veins and arteries are segmented from CT angiography or T1 weighted MRI with gadolinium enhancement using multi-scale, multimodal tensor voting"*. The tensor voting approach is a robust technique for extracting structures from a cloud of points. It is based on the assumption that a set of unconnected tokens (which are the primary characteristics of the image such as edges or figural components that stand out from the background; e.g. points) can exchange information within a neighbourhood that allows one to infer the geometric structure in which a token lies. In 3D, it provides a way to classify tokens, thus to estimate the likelihood that a token lies on a surface, curve or junction [46]. Tensor voting consists of three stages:

- *Token initialisation*

- *Tensor voting*

- *Analysis of voting results*

Token initialization   Information contained into token p is encoded in a tensor $\mathbf{T}$, which can be expressed as linear combination of three tensors:

$$\mathbf{T} = (\lambda_1 - \lambda_2)(\mathbf{e_1}\mathbf{e_1^T}) + (\lambda_2 - \lambda_3)\sum_{i=1}^{2} \mathbf{e_i}\mathbf{e_i^T} \qquad (2.34)$$

where λ_i are the eigenvalues of the tensor ordered by decreasing values and $\mathbf{e_i}$ the corresponding eigenvectors. The first term shows the eccentricity with orientation $\mathbf{e_1}$; the second term has the tangent $\mathbf{e_3}$ which represent a disk-shaped structure; the last term represents a ball tensor (a structure without orientation preferences).

Tensor voting After the decomposition of T in the 3 basic tensors, each token p propagates information to its neighbours in the form of a vote. The vote is a tensor that encode the direction of the normal at a neighbouring point.

Analysis of the voting results The result of a voting is another tensor which, for (2.34), can be decomposed to obtain 3 vector maps: the surface map (S-Map), the curve map (C-Map) and the junction map (J-Map). In addition to the tensor voting technique, the authors added a further data fusion step; they formulated the tensor voting approach into a multi-scale framework by evaluating the response of different scales at the data fusion stage and retaining the maximum response through scales. Finally, a vascular probability map is obtained and it is then used to identify the trajectories with a computer assisted automated planner.

In 2012 De Momi et al. [27] proposed a new automated planner for SEEG electrodes trajectory planning based on MRI and 3D Cone Beam CT Digital Subtracted Angiography (3D CBCT DSA).

In 2014 [10] they improved the planner introducing a multi-planner (MP) concept; with respect the previous work, in which the trajectories were computed depending only on the previous ones, the MP takes in account the spatial relationship of all the trajectories (independently on their insertion order) and then it computes best configuration of trajectories. The major drawback of this method was the computational inefficiency and the requested time to obtain the planning.

In 2017 Scorza et al. [36] continued the development of the planner described by De Momi et al. introducing two innovations:

- The use of an atlas to limit the searching space for the trajectories to the anatomical structures that surround the selected Entry Points and Target Points.

- The implementation of a brute force approach to overcome the previous problems

related to the electrode conflicts.

The planning procedure (Figure 2.13) is initialized by the loading of the patient images in order to generate available data used for trajectory optimization.
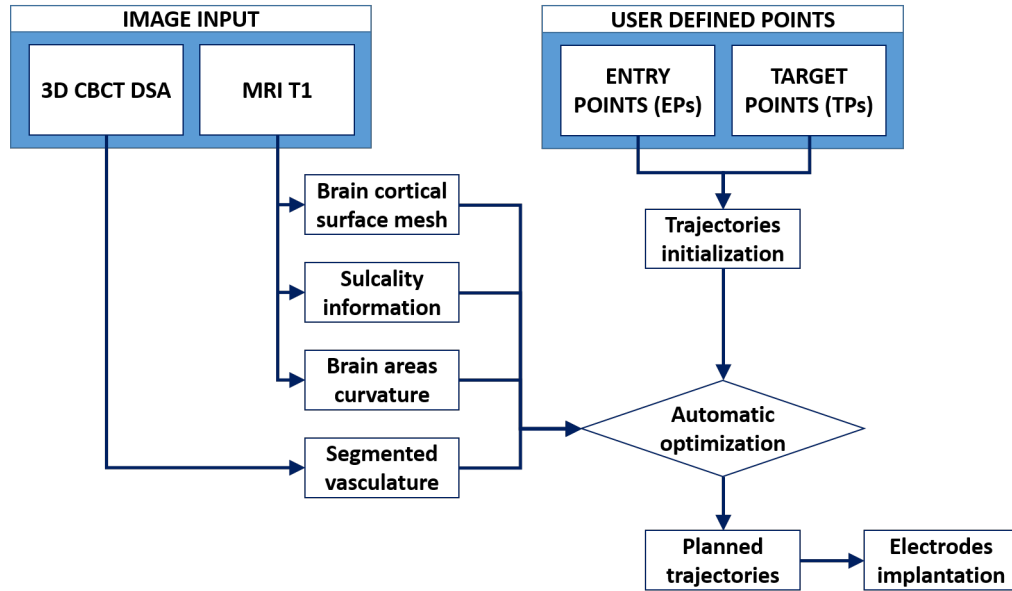

Figure 2.13: Example of automated planner workflow for SEEG electrodes implantation.

MRI T1 images are processed through Freesurfer pipeline in order to provide informations about cortex surface, sulcality and curvature of the brain areas. Then, 3D CBCT DSA (Figure 2.14) are used for vessel segmentation. DSA images are obtained into two phases[6]:

- first a CBCT volume of the patient (CT-bone) is preliminarly acquired in order to extract the bone-mask; then, another CBCT volume is acquired after the injection of a contrast medium.

- The two volumes are co-registerd, then, the final volume is obtained as a digital subtraction of the bone mask (preliminar volume) from the enhanced dataset (contrast enhanced volume). Thus, it allows to keep only the enhanced vascular tree.
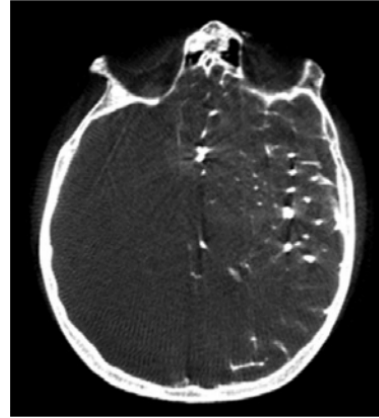
(a) Skull mask   (b) Enhanced dataset
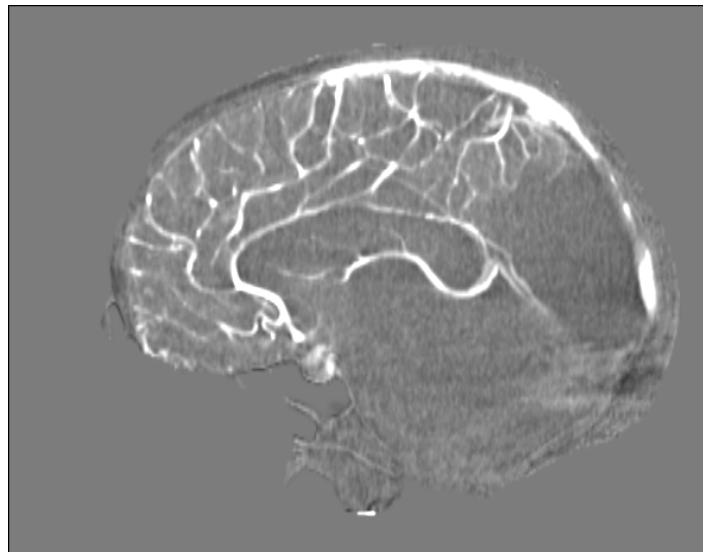
(c) DSA

Figure 2.14: Digital Subtracted Angiography (DSA). (**a**): the preliminar CT-bone is used to extract the binary mask of the skull. (**b**): the enhanced CT is acquired after the injection of the contrast medium. (**c**): the digital subtraction of the skull from the enhanced dataset produce the DSA.

Thanks to the DSA image, the segmentation can be achieved with a mono-modal threshold approach. Thus, the vessel binary mask is computed using a simple manual thresholding. So the user interactively selects the global threshold for the vessel segmentation based only a visual guidance of rendered volume.

The thresholding method resulted easy to use and very fast in comparison to other segmentation techniques. However, it presents some drawbacks such as:

- it is user-dependent;

- it does not include any morphological information;

- it could lead to noisy results or too skinny vessels (dangerous), especially in case of noised dataset.

2.3   Aim of the work

The brain vessels avoidance for automated planner in epilepsy surgery is one of the most important constraint. The manual segmentation of the 3D images is cumbersome, time consuming and subjective. Actually there are several automatic image segmentation methods, but the required accuracy and precision in minimally invasive brain surgery needs continuous improvements.

The aim of this work consists in the implementation of an automatic algorithm for vessel segmentation, based on GMM. The method proposed in [10] has been extended for 3D vascular segmentation in order to be included has an automatic segmentation step in the automated planning workflow [36].

Different methods have been developed and compared. Additionally, we performed experiments to define the best tuning of the algorithm parameters.

This work has been realized at Nearlab, Politecnico di Milano, under the supervion of the professor Elena De Momi through the collaboration with the team working at "Claudio Munari" Center for Epilepsy and Parkinson Surgery, Niguarda Ca' Granda Hospital, Milan, Italy, in particular the M.D. Francesco Cardinale, who made available data and clinical competences, and Davide Scorza, PhD candidate at Politecnico di Milano and Research Assistant at e-Health and Biomedical Applications Department, Vicomtech-IK4, Donostia-San Sebastian, Spain who has greatly contributed to the development of the project.

Chapter 3

Materials and methods

As introduced in chapter 1, vessels avoidance is one of the most important constraint to guarantee safety during SEEG. Thus, this work focuses on the development of three different fully-automatic algorithms for vessels segmentation of 3D CBCT DSA brain images and their performance evaluation.

The methods proposed are based on GMM approach, with an extension including neighbourhood through MRF and an additional implementation reproducing the work of R. Gan [15]. Finally, the methods are compared and they will be integrated in the automated planner workflow which is being developed in collaboration with "Claudio Munari" Center for Epilepsy and Parkinson Surgery (Niguarda Ca' Granda Hospital, Milan, Italy).

3.1 Proposed vessel segmentation methods

The clustering techniques can be effective to distinguish the structures of interest (vessels) from the rest of the image.
We used 3D CBCT DSA based on contrast medium enhanced images, so that the background is much darker than the enhanced vessel structures. However, the implemented GMM-based algorithms can be applied on other types of images (e.g. CE-MRI). The only constraint to be considered in changing type of images is to tune correctly the initialization parameter of the algorithm.

As stated in the actual state of the art (Chapter 2), among the clustering segmen-

tation methods there is a group of techniques based on the estimation of the data distribution with predefined models. A model-based approach consists in using certain models for clusters and attempting to optimize the fit between the data and the model. In practice, each cluster can be mathematically represented by a parametric distribution, like a Gaussian (continuous) or a Poisson (discrete). The entire data set is therefore modelled by a mixture of these distributions. An individual distribution used to model a specific cluster is often referred to as a *component* distribution.

3.1.1 Gaussian Mixture Model

A Gaussian Mixture Model (GMM) is a parametric probability density function represented as a weighted sum of Gaussian component densities. it is commonly used as a parametric model of the probability distribution of continuous measurements or features in several applications such as biometric systems (e.g. vocal-tract related spectral features in a speaker recognition system) or image segmentation. GMM parameters are estimated from training data using the iterative Expectation-Maximization (EM) algorithm or Maximum A Posteriori (MAP) estimation from a well-trained prior model[32].

Considering the problem of estimating the posterior probability of each observation at the i-th pixel x_i, with $i = 1, 2, ..., N$, belonging to the class Ω_j, with $j = 1, 2, ..., K$, the density function at an observation x_i is given by:

$$p(x_i) = \sum_{j=1}^{K} \pi_j p(x_i|\Omega_j) \tag{3.1}$$

where $p(x_i|\Omega_j)$ is a Gaussian distribution called *component* of the mixture, π_j is the prior distribution of the pixel x_i that belongs to the class Ω_j and satisfies the constraint:

$$\sum_{j=1}^{K} \pi_j = 1 \tag{3.2}$$

Each mixture component has its own mean μ_j and covariance σ_j and is given by:

$$p(x_i|\Omega_j) = \frac{1}{\sqrt{2\pi\sigma_j^2}} exp\left(- \frac{(x_i - \mu_j)^2}{2\sigma_j^2} \right) \tag{3.3}$$

The mean vectors, variance matrices and mixture weights are the main parameters that complete the GMM from all the component densities and are represented by the

notation:

$$\Theta = \{\Omega_j, \mu_j, \sigma_j\} \qquad j = 1, ..., K \tag{3.4}$$

The log-likelihood function of the GMM can be computed from the density function as:

$$L(\Theta) = \sum_{i=1}^{N} log\left(\sum_{j=1}^{K} \pi_j p(x_i | \Omega_j) \right) \tag{3.5}$$
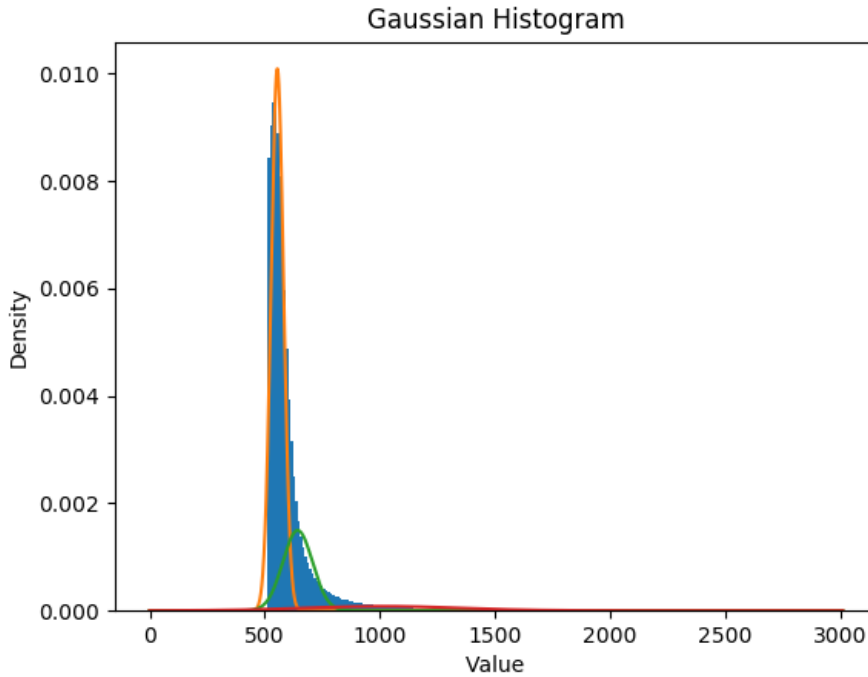

Figure 3.1: Example of GMM density distribution estimation using three Gaussian components.

As can be seen from the likelihood function in (3.5), one of the biggest advantages of the standard GMM is that it has a simple form and requires a small number of parameters (the *number of cluster* to estimate the intensity distribution and the *log-likelihood threshold* as the stopping criterion). However, the main drawback is that the pixel x_i is considered to be an independent sample. Therefore, it does not take into account the spatial correlation between the neighbouring pixels in the decision process[30]. In order to maximize the log-likelihood function, it is estimated with the iterative Expectation Maximization algorithm.

Expectation-Maximization algorithm

Maximum Likelihood Expectation-Maximization (ML-EM) algorithm can be used to estimate GMM parameters from training data. Suppose to have a data set of observations $\{x_1, ..., x_N\}$ and to wish to model this data using a mixture of Gaussians. If we assume that the data points are drawn independently from the distribution, then we can express the Gaussian mixture model for this independent and identically distributed data set. Thus, given the GMM, the goal is to maximize the likelihood function with respect to the parameters (comprising the means and covariances of the components and the mixing coefficients).

The ML-EM algorithm can be summarized in four major steps:

1. **Parameters initialization**: first the means μ_j, the covariance σ_j and the mixing coefficients Ω_j are initialized and the initial value of the log-likelihood is set.

2. **Expectation step (E-step)**: during this step, the so called *posterior probability* is computed using the current parameter values (λ).

$$p^{(t)}(\Omega_j|x_i) = \frac{\pi_j^{(t)} p^{(t)}(x_i|\Omega_j)}{\sum_{l=1}^K \pi_l^{(t)} p^{(t)}(x_i|\Omega_l)} \tag{3.6}$$

3. **Maximization step (M-step)**: this step re-estimates the parameters using the current responsibilities computed in E-step.

$$\pi_j^{(t+1)} = \frac{1}{N} \sum_{i=1}^N p^{(t)}(\Omega_j|x_i) \tag{3.7}$$

$$[\sigma_j^2]^{(t+1)} = \frac{\sum_{i=1}^N p^{(t)}(\Omega_j|x_i)[x_i - \mu_j^{(t+1)}]^2}{\sum_{i=1}^N p^{(t)}(\Omega_j|x_i)} \tag{3.8}$$

$$\mu_j^{(t+1)} = \frac{\sum_{i=1}^N p^{(t)}(\Omega_j|x_i)x_i}{\sum_{i=1}^N p^{(t)}(\Omega_j|x_i)} \tag{3.9}$$

where t is the iteration step.

4. **Log-likelihood evaluation**: The log of the likelihood is computed with equation (3.5). If the log-likelihood reached the convergence the algorithm stops, otherwise, if the convergence criterion is not satisfied, it returns to step 2 until the convergence or the maximum number of iterations is reached.

45

There is a significant problem associated with the maximum likelihood framework applied to GMMs, due to the presence of singularities. For simplicity, consider a GMM whose components have covariance matrices given by $\boldsymbol{\sigma_i} = \sigma_i \boldsymbol{I}$, where $\boldsymbol{I}$ is the unit matrix, although the conclusions will hold for general variance matrices. Suppose that one of the components of the mixture model has its mean μ_j exactly equal to one of the data points so that $\mu_j = x_i$ for some value of i. This data point will then contribute a term in the likelihood function of the form:

$$p(x_i|x_i, \sigma_j \boldsymbol{I}) = \frac{1}{\sqrt{2\pi\sigma_j^2}} \tag{3.10}$$

If we consider the limit $\sigma_j \to 0$, then this term goes to inf and so the log-likelihood function will also go to inf. Thus the maximization of the log-likelihood function is not a well posed problem because such singularities will always be present and will occur whenever one of the Gaussian components "collapses" onto a specific data point[5]. The singularities problem can be avoided by using suitable heuristics (e.g. by detecting when a component is collapsing and reset its mean to a random value and its variance to a large value) or using Maximum A Posteriori (MAP) solutions for GMM in which a prior is defined over the parameters. One of the main drawback of this method is that the prior distribution π_j does not depend on the pixel index i and thus, not on the spatial relationship between the labels of neighbouring pixels. Thus, the segmentation is extremely noise prone and illumination dependent[40]. To overcome this disadvantage, mixture models with Markov Random Field (MRF) have been employed for pixel/voxel labeling.

3.1.2 Gaussian Mixture Models with Markov Random Field

Generally, in images, the neighbouring pixels are highly correlated if they belong to the same object. If the correlation is not used, the segmentation can be very sensitive to noise, varying illumination and other environmental factors. Markov Random Field (MRF) was introduced for GMM segmentation in order to use this spatial information. The density function at an observation x_i is given by:

$$p(x_i) = \sum_{j=1}^{K} \pi_{ij} p(x_i|\Omega_j) \tag{3.11}$$

where the prior distribution π_{ij} of the pixel x_i that belongs to the class Ω_j satisfies the constraints:

$$\pi_{ij} = p(\Omega_i | \Omega_{N_i}, \beta) \quad \& \quad \sum_{j=1}^{K} \pi_{ij} = 1 \tag{3.12}$$

Thus the prior π_{ij} is different for each pixel/voxel i and depends on its neighbours and the parameter β that expresses the importance of the neighbourhood intensities (the parameters *beta* and *neighbourhood* are initialized by the user with the *number of cluster* and the *log-likelihood threshold*).

The log-likelihood can be re-written as:

$$L(\Theta) = \sum_{i=1}^{N} log\left(\sum_{j=1}^{K} p(x_i | \Omega_j) p(\Omega_i | \Omega_{N_i}, \beta) \right) \tag{3.13}$$

With respect to the standard GMM, the log-likelihood function has a simpler form. The main advantage of this technique is that it embodies spatial dependencies between pixels/voxels that allows to take into account the characteristics of the whole object and not only of the single pixel/voxel. The main drawback is the time needed for the algorithm to reach the convergence that is much more longer than the standard GMM.

3.1.3 GMM with MRF based on Maximum Intensity Projection

In 2005 R. Gan et al. [15] proposed a novel vessel segmentation approach based on Maximum Intensity Projections (MIP). They observed that the volume occupied by the vessels in clinical 3D-Rotational Angiography (3D-RA) typically is very small. Thus, the imbalance between proportions of two classes (vessel and non-vessel/background) makes the estimation of the intensity distribution very difficult. In fact, the Gaussian component that corresponds to the vessels may shift to lower intensity range because of the EM algorithm. Thus causes a relatively low threshold selection and it produces an oversegmented image as result. To deal with this problem they proposed an iterative approach to segment 3D-RA images progressively with the segmentation of the MIP images along the three principal axes and the final result is a combination of the results obtained along the individual axes using a winner-takes-all strategy. In order to improve the parameter estimation of Finite Mixture Model (FMM) with the EM

algorithm, they suggest that the parameters of FMM should not be estimated with the whole 3D volume. Instead, the parameter estimation is performed with MIP images of the volume. The MIP image is a 2D projection of a 3D volume, where the intensity value assigned to a pixel is the highest one found in the 3D volume along the projection line. Because of the nature of the MIP image formation, it is an effective visualization tool if the objects of interest are brighter than the unwanted structures in the volume. Such property of MIP allows to estimate the parameters of the FMM more robustly. Moreover, they assert that *"because of the increase in the proportion of vessels in MIP images, the intensity distribution of vessels can be approximated more accurately"*[15]. The method can be summarized in few steps:

1. The algorithm starts with the generation of a MIP image from the original 3D volume along one of the three principal and orthogonal axes to avoid intensity interpolation.

2. The obtained MIP is then segmented using the ML-EM method explained in section 3.1.2 with a double-Gaussian mixture modelto approximate the MIP intensity distribution.

3. At each iteration, the 3D position of the voxel that contributed to the MIP is recorded and the voxels corresponding to the MIP pixel classified as a vessel, is saved to the segmented 3D volume and then the original voxel is removed from the original 3D volume to not contribute more to the MIP image generation at the following iteration.

4. During the next iteration a new MIP is generated from the 3D volume (with the exclusion of the voxels used at the previous iteration) and then the point 2 and 3 are repeated until the convergence or the maximum number of iteration are reached.

5. The algorithm is applied along the three different principal axes so that, at the end, it gives three different segmented volumes. The final result is the fusion of these three different volumes using a winner-takes-all strategy.

The stopping criterion

As the intensity distribution of the MIP image is evolving through the iterations and the number of high-intensity voxels decreases as the algorithm proceeds, a stopping criterion is needed.

Gan et al. proposed an automatic mechanism to detect the left-shift of the Gaussian component with a higher mean to the lower-intensity region. Let h_k^B be the estimated background instensity distribution at the iteration k obtained using the threshold computed at the previous iteration (t_{k-1}):

$$h_k^B(i) = \begin{cases} h_k(i), & \text{if } i < t_{k-1} \\ 0, & \text{otherwise} \end{cases} \tag{3.14}$$

where h_k is the observed intensity distribution of the MIP at iteration k and i is the intensity value. Let h_k^G be the estimated Gaussian component with the lower mean in the GMM and $h_k^G G$ be the overall distribution of the double-Gaussian mixture model. The proposed automatic mechanism computes the Sum of Absolute Differences (SAD) between h_k^B and the other two distributions h_k^G and $h_k^G G$. So the results can be summarized as SAD (h_k^B, h_k^G) and SAD$(h_k^B, h_k^G G)$ respectively. Then, the differences between the two SADs are evaluated. Thus, the algorithm stops when the Gaussian component with higher mean left-shifts below the Gaussian component with lower mean, so that when:

$$SAD(h_k^B, h_k^G) > SAD(h_k^B, h_k^G G) \tag{3.15}$$

According to the proposed stopping criterion, *"the only condition that makes the algorithm fail to converge and terminate is that the left-shift of the Gaussian distribution with a higher mean never occurs. In other words, a severe imbalance between the proportions of the vessels and the background never occurs for the MIP image"*[15].

The proposed algorithm was then extended to multiple projections along the three principal orthogonal axes. Thus the process is used to obtain three different segmented volumes and then the Iterated Conditional Model (ICM) is used to minimize an energy function $E_{(x)}$:

$$E_{(x)} = \sum_{v \in V} \left(L(X_v | I_v) + \lambda \sum_{v' \in N_{(v)}} P(X_v, X_{v'}) \right) \tag{3.16}$$

49

where X_v is the classification of a voxel v in X as vessel or background, I_v is the observed intensity value of v, λ controls the degree of spatial smoothness and $P(X_v, X_{v'})$ is:

$$P(X_v, X_{v'}) = \begin{cases} -1, & \text{if } X_v = X_{v'} \\ 0, & \text{if } X_v \neq X_{v'} \end{cases} \tag{3.17}$$

and $L(X_v|I_v)$ is:

$$L(X_v|I_v) = \frac{1}{\chi_D} \sum_{x \in \chi_D} L_x(X_v|I_v) \tag{3.18}$$

where $L_x(X_v|I_v)$ is the negative log-likelihood energy of classification X_v to intensity value I_v in segmentation $x \in \chi_D$
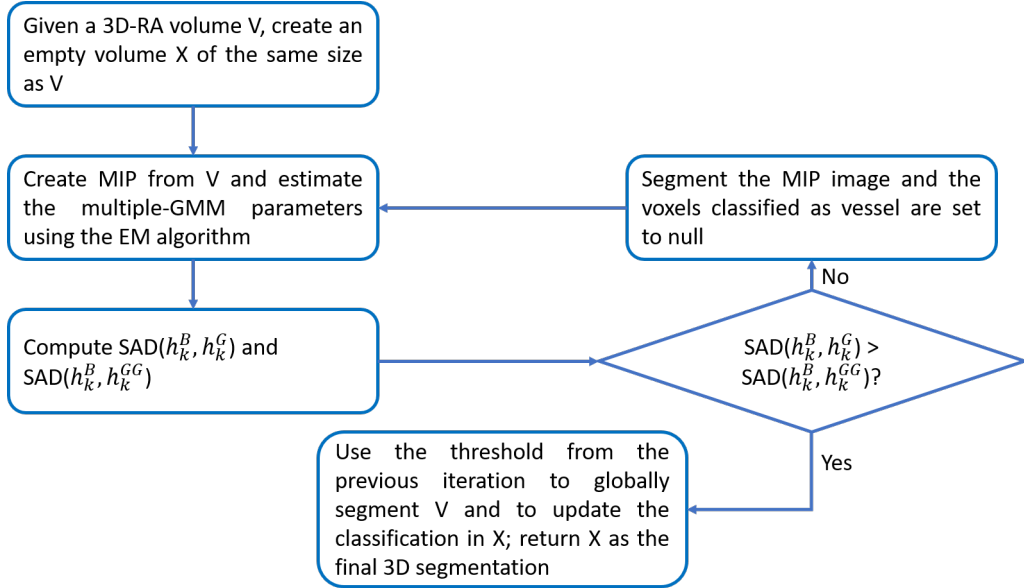
Figure 3.2: Workflow of the GMM based on MIP segmentation of R. Gan 2005 [15]

3.1.4 Image preprocessing

Before the segmentation, the images are pre-processed in order to reduce the timing and the computational cost and to increase the signal to noise ratio (SNR).

First a *cropping on the region of interest (ROI)* (Figure: 3.3) is applied in order to reduce the processed data. The volume is automatically cut in order to obtain the minimum parallelepiped that contains the brain.

When the surgery regards only one hemysphere (mono-lateral surgery), the ROI cropping, after a correction of the volume orientation, is done into two phases:

1. Separate the volume into two parts: the volume is divided into two halfs with respect to the sagittal plane of the patient head, thus dividing the brain into the two hemispheres.

2. Cut the ROI: the weighted intensity means of the two volumes are calculated. Because the ROI contains enhanced vessels, the intensities in that ROI are higher with respect to the rest of the volume. So, the hemisphere with the highest mean is selected because it corresponds to the part containing the ROI. The selected half is then cut in order to obtain the minimum parallelepiped that contains the brain hemisphere.

(a) Image   (b) ROI
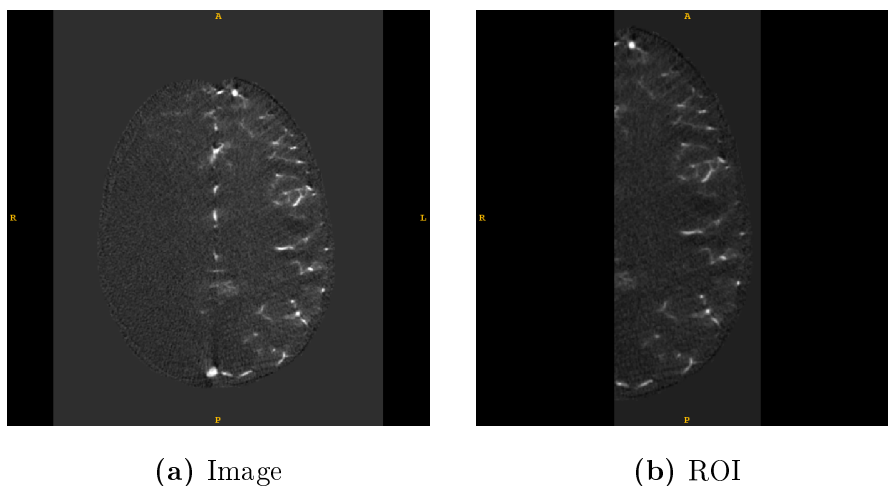
Figure 3.3: Left: usual CBCT DSA image that contains the whole head of the patient with a hemisphere with enhanced vessels. **Right**: ROI considered for the segmentation

Then, an *intensity threshold* is applied; because of the contrast medium, vessel structures present intensity values considerably higher with respect the background. Additionally, looking to the image histogram (Figure 3.4), it is possible to notice a high peak in correspondence of 0-value. The peak is caused by the substraction of co-registered images when obtaining the DSA. Moreover, such a high spike could lead the GMM-based segmentation methods to an erroneous estimation and then to diverge. Consequently, we decide to apply a threshold which eliminates all voxel values ≤ 0, since we assume that all the vascular information is represented by higher intensities.

(a) Before Thresholding   **(b)** After Thresholding
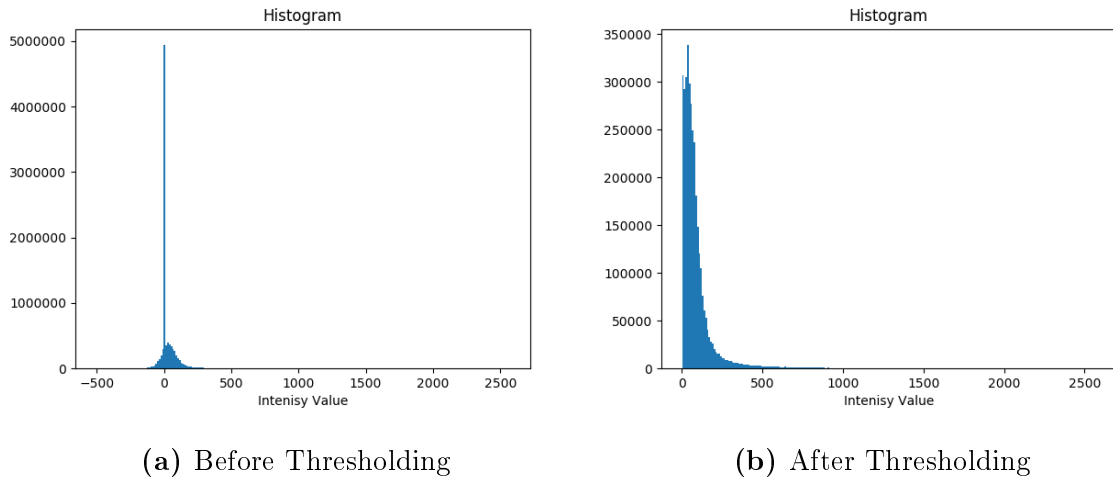
Figure 3.4: Left: The intensity histogram of the patient volume shows the highest peak at the zero intensity value. It corresponds to the number of voxels that represent the air surrounding the patient's head. **Right**: After threshold application the distribution is more likely Gaussian-shaped, thus can be better estimated by GMM.

Then the intensities are rescaled basing on the range of the intensities. Thus, it allows to estimate the Gaussian in a faster way.

3.2 Experimental setup

We performed two different experiments: the first to define the optimum parameters to apply to GMM and GMM-MRF algorithms in order to obtain the vascular segmentation; then, we select the parameters which provided the best results, and used them to compare the different methods. We used a manual segmentation performed by an expert as ground truth. For each segmentation method, we computed the following indices against that ground truth: Sensitivy, Specificity, Precision, Accuracy and Dice smilarity coefficient (DSC).

3.2.1 Image dataset

Patient dataset This study involved an anonymized dataset of six patients provided by the team working at the "Claudio Munari" Center for Epilepsy and Parkinson Surgery, Niguarda Ca' Granda Hospital in Milan. The dataset included 3D CBCT

DSA acquired with the mobile CBCT device O-arm® 1000 System (Medtronic Inc., Minneapolis, Minnesota, US, matrix $512 \times 512 \times 192$, voxel $0.4mm \times 0.4mm \times 0.8mm$). The baseline dataset for the DSA was acquired after the injection of the iodinate contrast medium.

Segmented dataset All the patients had a mono-lateral injection of contrast medium, hence we automatically estimated the ROI and performed the thresholding considering only one hemisphere.

The implemented segmentation methods have been applied to all the images of the dataset using all the different combinations of initialization parameters. The considered parameters are:

- Number of cluster: it initializes the number of cluster in which the voxel are classified;

- Log-likelihood threshold: it sets the threshold for the convergence of the segmentation methods;

- Beta: it expresses the importance of the neighbour voxels for the segmentation with GMM-MRF;

- Neighbourhood: it sets the number of considered neighbouring voxels for the segmentation with GMM-MRF.

Ground truth dataset The ground truth dataset was then created manually segmenting the six volumes of the provided patient dataset. Because the manual segmentation is highly time-consuming ($8 \div 10$ hours per volume), for each patient, four different subvolumes were manually segmented by an expert surgeon:

- Three subvolumes with dimensions 20 x 20 x 10: one near the temporal lobe (called "Temporal"), one near the occipital lobe (called "Occipital") and one near the frontal lobe (called "Frontal"); these volumes contains short branches of vessels of small-medium width, thus to evaluate the capability of the segmentation method to identify the smallest vessels.

- One subvolume with dimensions 70 x 70 x 70: this volume (called "Combined") contains vessels with different calibers.

Even though it requested $\sim$ 2 hours per patient, segmenting different anatomical areas allowed us to avoid errors due to peculiarities of each volume. Moreover, build subvolumes respecting anatomical areas for each patient allowed to compare and to generalize the results.
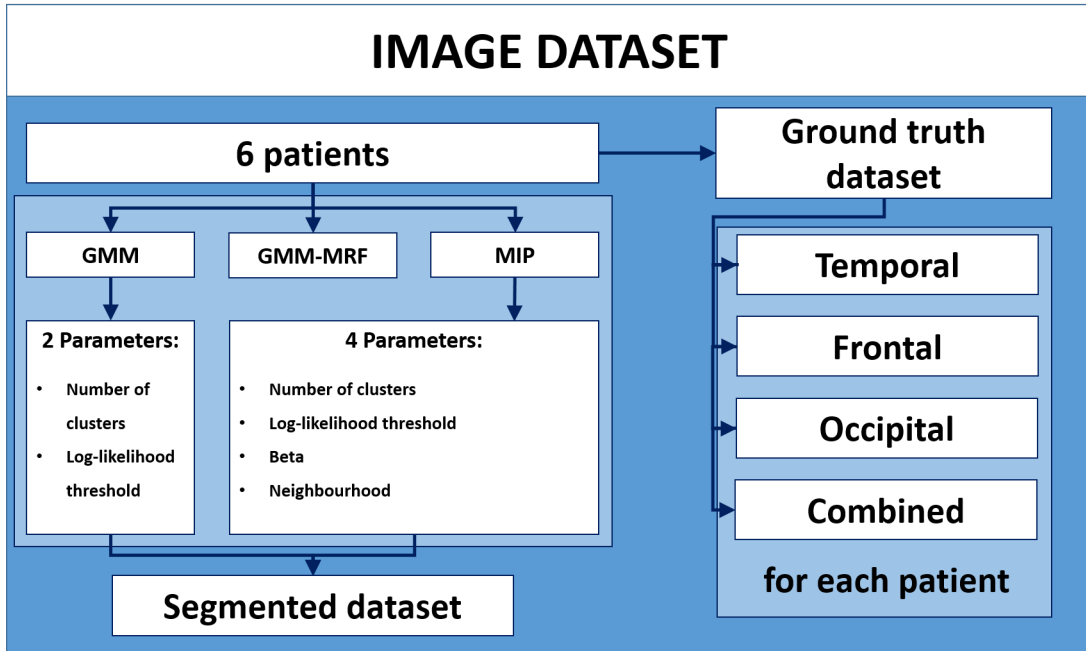

Figure 3.5: The segmented dataset contains the volumes segmented with all the developed algorithms. The ground truth dataset contains manually segmented volumes (four for each patient).

3.2.2 Algorithm evaluation

To evaluate the three different vessel segmentation algorithms, two different experiments were done:

1. **Parameters tuning**: each one of the segmentation method has different parameters to be set for the algorithm initialization. The tuning of each parameter is done in order to select the best parameter combination for each single technique.

2. **Algorithm comparison**: once the best parameter combination of each algorithm has been found, the algorithm can be compared in order to identify the

best segmenttion method.

3.2.3   Definition of optimal parameters

Because different combinations of parameters lead to very different segmentation results, it is necessary to identify the optimal parameters to reach the best result. The parameters tuning experiments were done on volumes segmented with GMM and GMM-MRF algorithms. The segmentation method based on MIP was not tuned because it relies on the GMM or the GMM-MRF technique. Thus, the best method and combination of parameters will be used also for the method based on MIP.

The beta and neighbourhood parameters are only for GMM-MRF segmentation algorithm, thus the dataset of images segmented with GMM was excluded from the tuning of these parameters. Each dataset was then compared with the ground truth dataset to obtain the confusion matrix and compute the evaluation indices described in paragraph 3.2.5.

We did the tuning experiments testing one parameter at a time with the different selected values. We tested all the combination of parameters, but only the relevant ones will be presented.

Number of cluster

The number of cluster defines the number of the Gaussian components which estimates the intensity distribution, so the classes in which the voxels are classified. Looking at the different volumes 2 clusters can be sufficient to identify what is *"vessel"* and what is *"background"*. However, a higher number could help to classify darker or smaller vessels. Thus we consider also segmentation with 3 and 4 clusters.

Binarization cluster threshold

The segmented data for automated planners must be binarized in order to be used for the planning optimization. Because the dataset contains data segmented with more than two classes, we identified the threshold on the number of cluster to make sure that the binarization is best performed.

Log-likelihood threshold

Because the implemented segmentation algorithms are based on iterative techniques, the log-likelihood threshold sets the limit for the convergence. When the difference of the log-likelihood between two iterations is lower than the selected threshold the method reached the convergence (it is a measure of goodness of the gaussian fitting of the data). The lower the threshold, the better the fitting is, but the longer the segmentation time is. Because of the volume dimension, we considered a log-likelihood threshold of 10 and 100 (lower thresholds need higher computational timing).

Beta

This parameter expresses the importance of the neighbouring voxels for the segmentation methods with GMM-MRF. Looking at the segmented images we selected the beta values of 1.2, 1.5 and 1.8.

Neighbourhood

This parameter sets the number of neighbouring voxels to be considered to compute the energy function that optimizes the classification of the condered voxel with the GMM-MRF method. The considered neighbouring voxels are 18 and 26.

3.2.4   Algorithm comparison

Once the combination of parameters of each vessel segmentation algorithm has been selected, the developed methods were compared to evaluate the one that gives the best segmentation. In addition, the patient volumes were segmented with a manual threshold by an expert in order to compare the developed algorithms with respect to the actual method used by De Momi et al. in their planner.

The segmented dataset was then compared with the ground truth dataset to obtain the confusion matrix and to compute the evaluation indices described in paragraph 3.2.5. The comparison was also done with respect to the time requested for each segmentation method. The timing of the segmentation methods must be less then 5 hours to be considered as acceptable.

3.2.5   Evaluation indices

To evaluate the obtained confusion matrices, five indices were used: Sensitivity (Sens), Specificity (Spec), Precision (Prec), Accuracy (Acc) and Dice similarity coefficient (DSC). These indices were computed after the calculation of the confusion matrix obtained by comparing the segmented volumes with the implemented methods with respect to the gold standard given by the manual segmentation performed by an expert.

Figure 3.6: The confusion matrix show the performance of the classification algorithms.

A true positive (TP) is a pixel belonging to the vessels' class which is properly classified in the segmented image. A true negative (TN) is a pixel belonging to the background's class which is properly classified in the segmented image. A false positive (FP) is a pixel belonging to the background's class which is wrongly classified as a vessel in the segmented image. A false negative (FN) is a pixel belonging to the vessels' class which is wrongly classified as a background in the segmented image. Once obtained the confusion matrix (Figure 3.6), the above described indices are then computed to assess the quality of the segmentation.

Sensitivity   It is the proportion of true positives that are correctly identified (it is also known as the True Positive Rate). It shows how good the algorithm is at detecting vessels. The higher the numerical value of sensitivity, the less likely segmentation returns false-positive results.

$$Sens = \frac{TP}{TP + FN} \tag{3.19}$$

Specificity   It is the proportion of the true negatives correctly identified (it is also known as the True Negative Rate). It suggests how good the algorithm is at identifying the background. A segmentation can be very specific without being sensitive, or it can be very sensitive without being specific. Both factors are equally important. A good segmentation has both high sensitivity and specificity.

$$Spec = \frac{TN}{TN + FP} \tag{3.20}$$

Precision   It is the proportion of positive results that are true positive (it is also known as Positive Predictive Value). The higher the precision value, the better the vessel boundaries are segmented.

$$Prec = \frac{TP}{TP + FP} \tag{3.21}$$

Accuracy   It is the proportion of true results, either true positive or true negative, in a population. It measures the degree of veracity of a segmentation. The higher the accuracy value, the better thinner vessel are segmented.

$$Acc = \frac{TP + TN}{TP + FP + TN + FN} \tag{3.22}$$

DSC   Dice coefficient is often used to quantitavely describe the capability of a segmentation algorithm to identify the regions with particular shapes and dimensions. In particular the value of a DSC ranges from 0, indicating no spatial overlap between two sets of binary segmentation results, to 1, indicating complete overlap.

$$DSC = \frac{2|\Omega_1 \cap \Omega_2|}{|\Omega_1| + |\Omega_2|} \tag{3.23}$$

To simplify the expression, it can be rewritten as:

$$DSC = \frac{2TP}{2TP + FP + FN} \tag{3.24}$$

It gives more weight to true positives, thus, in case of the vessel segmentation images analysis, to the pixels/voxels properly classified as vessels.

Because of the small number of available clinical data for our experiments, we can't prove the results with a statistical analysis. So, the final conclusions are based on a summarized evaluation of the results supported by the opinion of an expert surgeon.

Chapter 4

Results

In this chapter the results achieved with the different segmentation methods are presented.

The confusion matrix are computed comparing the dataset segmented with the developed algorithms and the ground truth manually segmented. Thus, for each segmented data, four confusion matrix were built (one for each ground truth). Then, to summarize the data, the total confusion matrix was computed as the sum of the four previously described. Finally, the evaluation indices were computed on the total confusion matrix.

The first section reports the indices relative to the parameters tuning experiments. The second section summarizes the results of the comparison between the different vessel segmentation algorithms with the best combination of parameters.

4.1 Parameters tuning results

This paragraph reports the results for the tuning of the parameters for both the GMM and GMM-MRF segmentation methods.

4.1.1 Results GMM

Results GMM: cluster binarization threshold

3 cluster The figure 4.1 shows the boxplots of the evualuation indices computed on the images segmented with GMM initialized with 3 clusters.

The Sensitivity shows a higher median on the threshold set on the cluster 1 (0.99) with respect to the threshold on the cluster 2 (median 0.68) that has a higher interquantile range (IQR). However, the threshold on the cluster 2 has higher median with a comparable IQR for all the other indices. Thus, because of the presence of a very high number of FP and TP with respect the number of FN.

(a) Sensitivity

(b) Specificity

(c) Precision

(d) Accuracy

GMM: 3 cluster binarization threshold
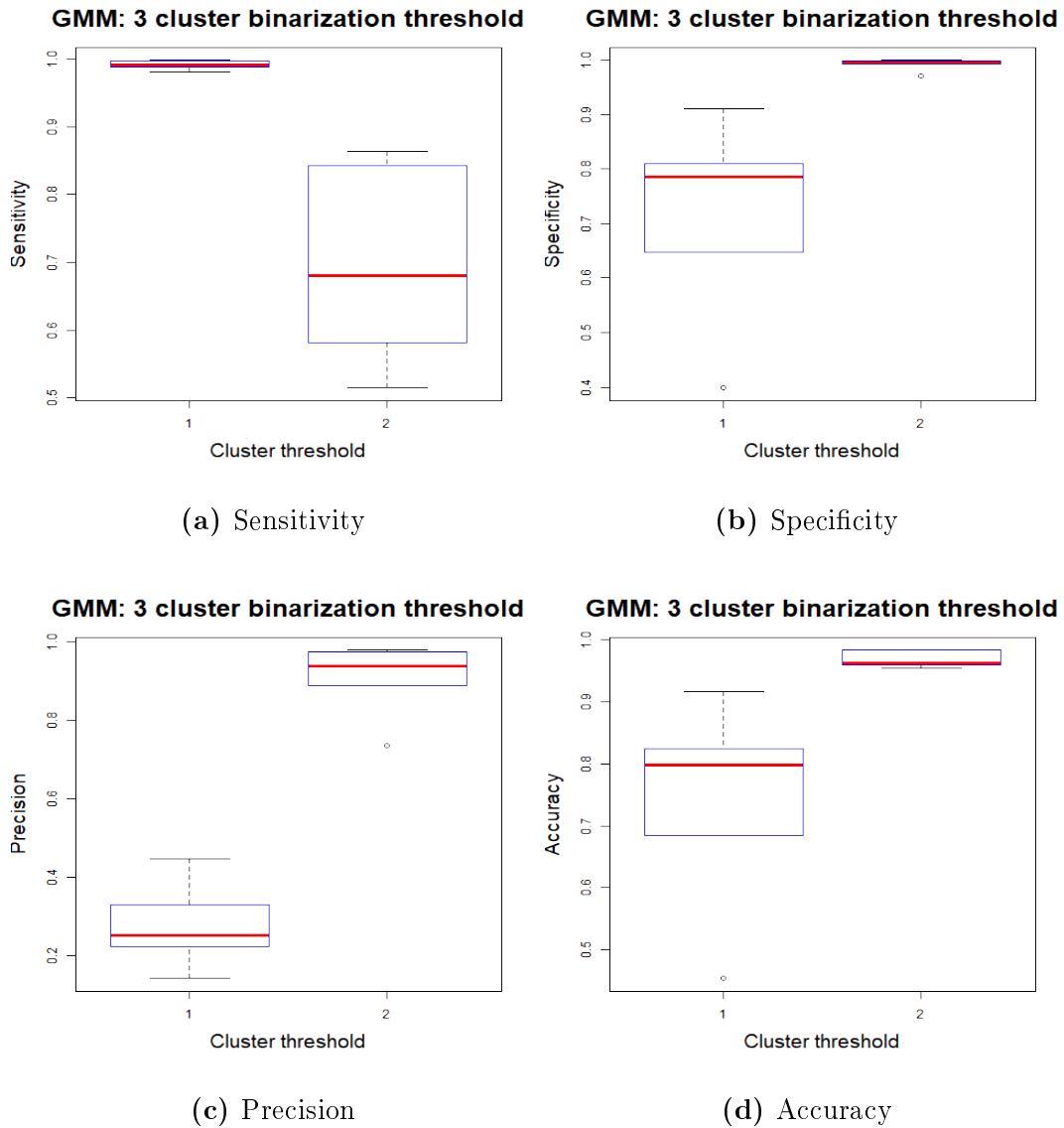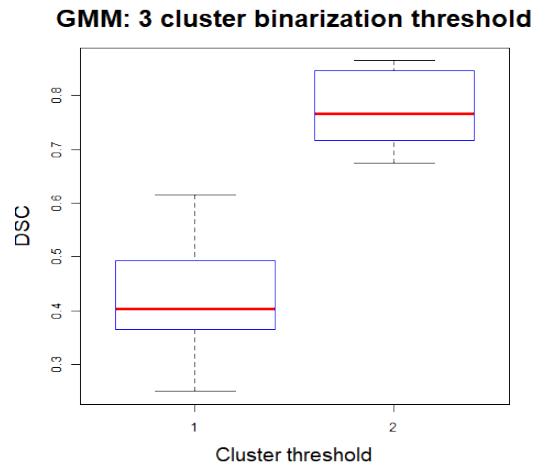
(e) DSC

Figure 4.1: GMM results: 3 cluster binarization threshold. Box plots of **(a)** Sensitivity, **(b)** Specificity, **(c)** Precision, **(d)** Accuracy and **(e)** DSC for the binarization threshold.

4 cluster   The figure 4.2 shows the boxplots of the evualuation indices computed on the images segmented with GMM initialized with 4 clusters.
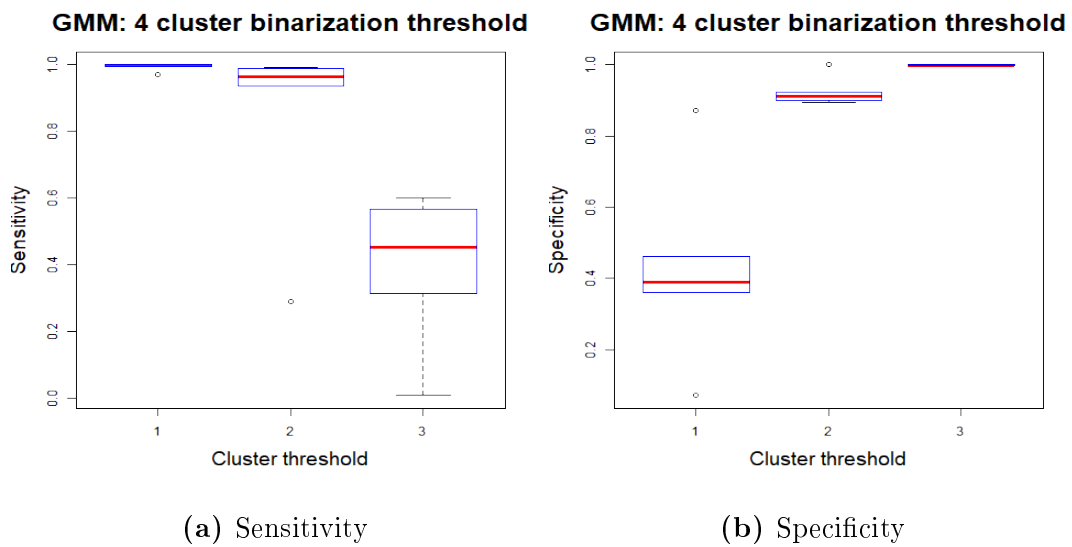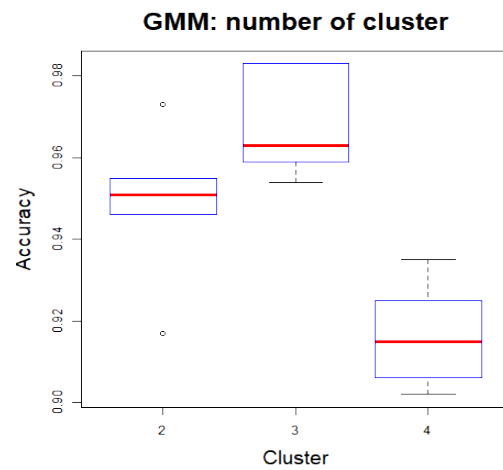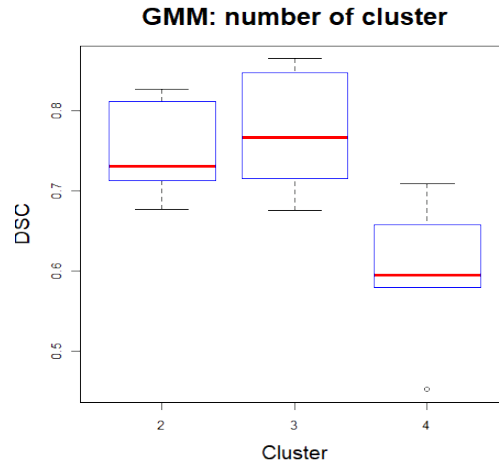

(a) Sensitivity
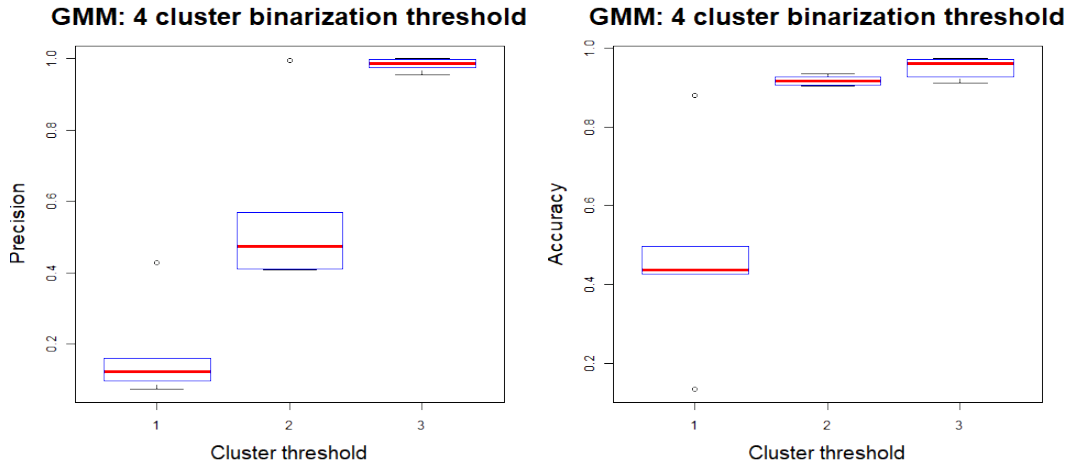
(b) Specificity

(c) Precision   **(d)** Accuracy
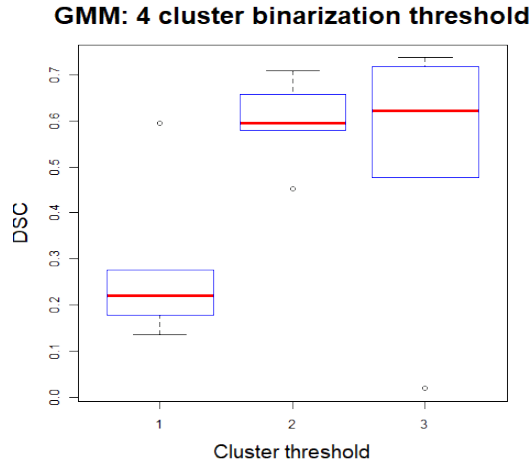
(e) DSC

Figure 4.2: GMM results: 4 cluster binarization threshold. Box plots of **(a)** Sensitivity, **(b)** Specificity, **(c)** Precision, **(d)** Accuracy and **(e)** DSC for the binarization threshold.

The Sensitivity has higher values for the binarization threshold set to 1 for each patient (with a median value of ~ 0.99), but the other coefficients have very low values with respect to the other thresholds; in fact, with threshold 1, the segmentations have a very high number of FP. Specificity, Precision and Accuracy are higher with the threshold set to 3, but with a low value of Sensitivity because of a little number of TP with respect to the FN. The threshold 2 shows medium values of Precision and DSC (median values of 0.47 and 0.56 respectively) with respect the other thresholds, but it still has high values of Sensitivity, Specificity and Accuracy (median values of 0.96,

0.91 and 0.92 respectively) with a very small IQR.

Results GMM: number of cluster

The figure 4.3 shows the boxplots of the evualuation indices computed on the images segmented with GMM for the tuning of the number of cluster.
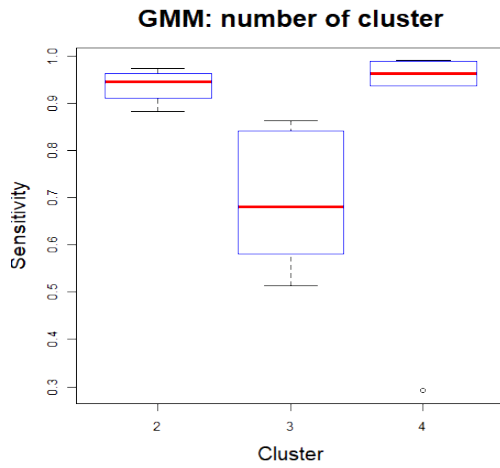
(a) Sensitivity
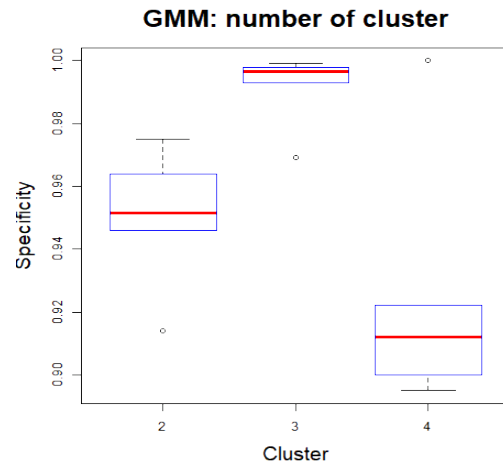
(b) Specificity
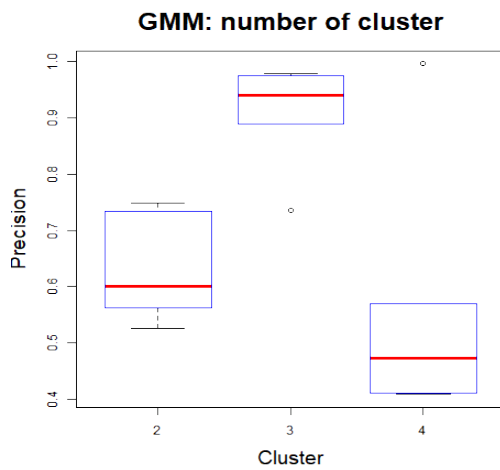
(c) Precision

(d) Accuracy

(e) DSC

Figure 4.3: GMM results: number of cluster. Box plots of **(a)** Sensitivity, **(b)** Specificity, **(c)** Precision, **(d)** Accuracy and **(e)** DSC for the tuning of the number of cluster.

The Sensitivity has high and comparable median and IQR for 2 and 4 clusters, but a slightly smaller value for 3 cluster with a larger IQR. Despite the high sensitivity, the segmentation with 4 cluster shows lower medians for all the other indices with a comparable IQR with respect to the 2 and 3 clusters. In fact, despite the high number of TP and TN, the FP are high. Specificity, precision, accuracy and DSC have higher medians for the segmentations with 3 cluster (with values of $\sim$1, 0.94, 0.96 and 0.77 respectively), but with a lower value of Sensitivity because of a higher number of FN.

Results GMM: log-likelihood threshold

The figure 4.4 shows the boxplots of the evualuation indices computed on the images segmented with GMM for the tuning of the log-likelihood threshold.

All the indices shows a IQR similar for the tested log-likelihood threshold, but Sensitivity, Accuracy and DSC show higher median values for the segmentations with a log-likelihood threshold of 10 with a value of 0.72, 0.97 and 0.78 respectively. Specificity and Precision have a slightly higher median for the threshold set to 100 ($\sim$1 and 0.94 respectively).
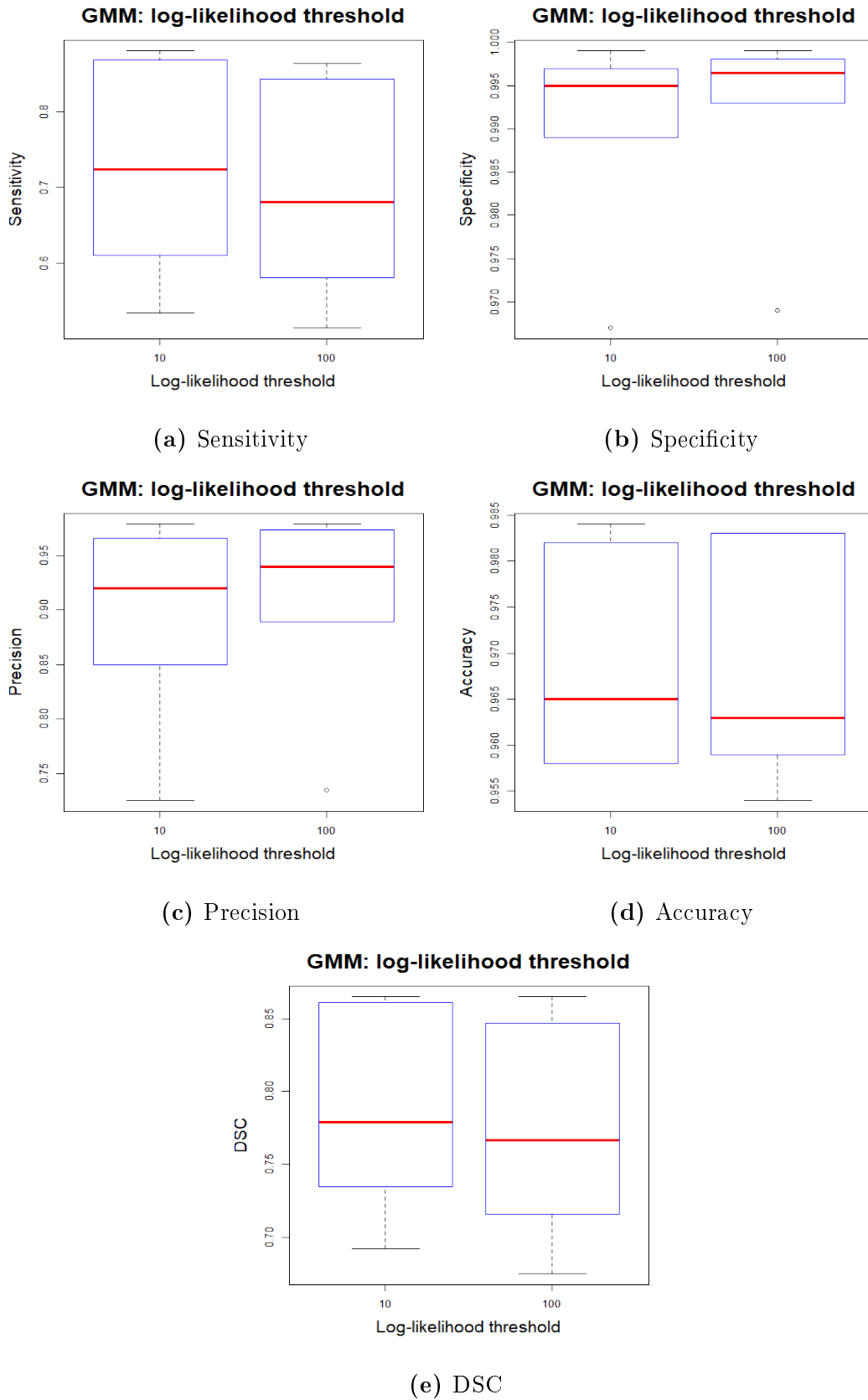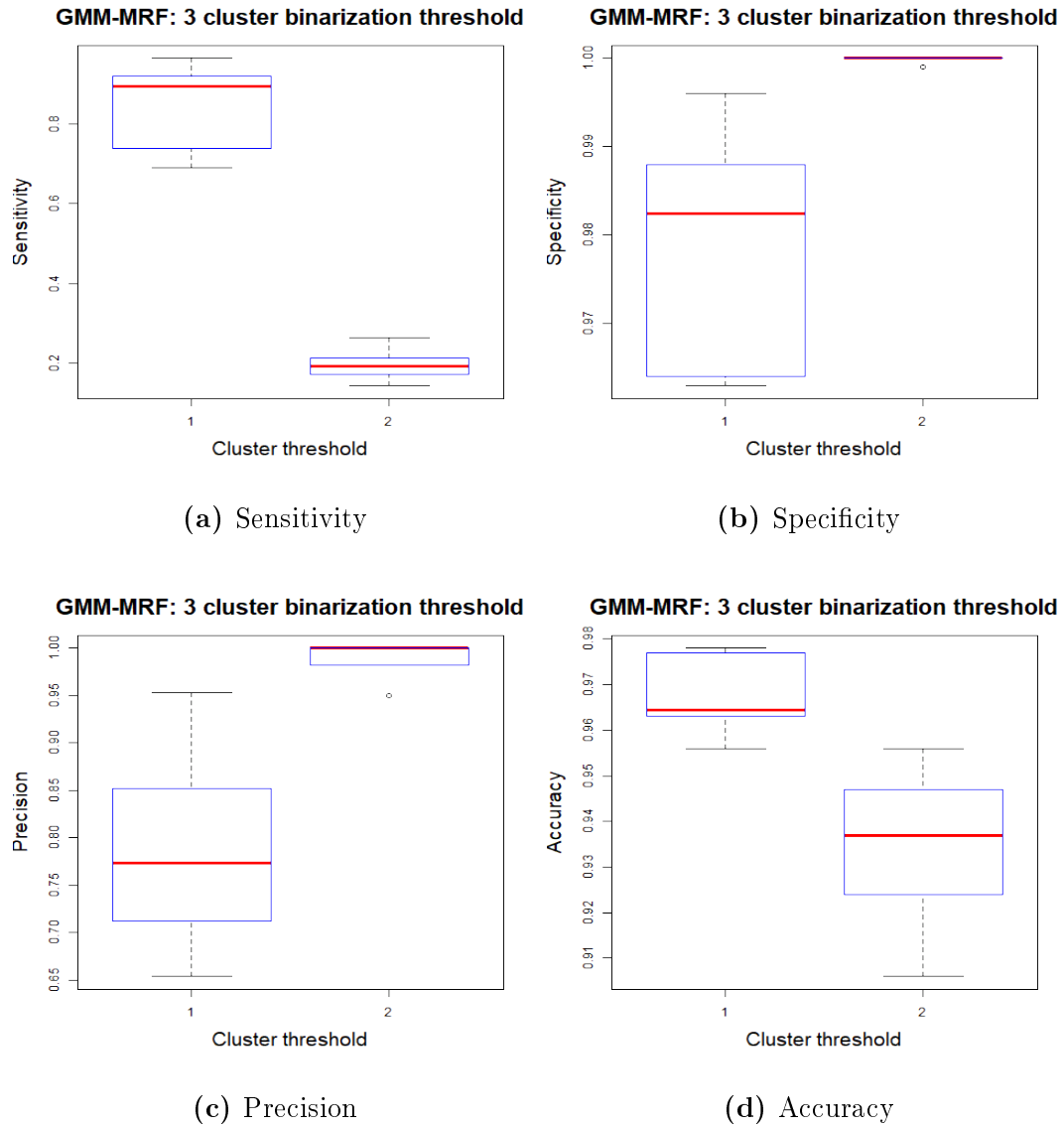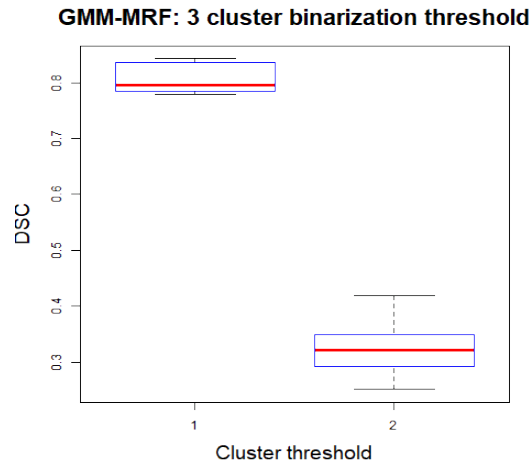
64

(a) Sensitivity

(b) Specificity

(c) Precision

(d) Accuracy

(e) DSC

Figure 4.4: GMM results: log-likelihood threshold. Box plots of **(a)** Specificity, **(b)** Sensitivity, **(c)** Precision, **(d)** Accuracy and () DSC for the tuning of the log-likelihood threshold.

4.1.2 Results GMM-MRF

Results GMM-MRF: binarization cluster threshold

3 cluster   The figure 4.5 shows the boxplots of the evualuation indices computed on the images segmented with GMM-MRF initialized with 3 clusters.
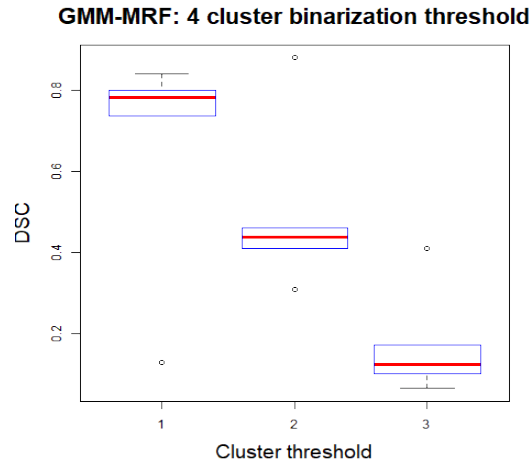

(a) Sensitivity

(b) Specificity

(c) Precision

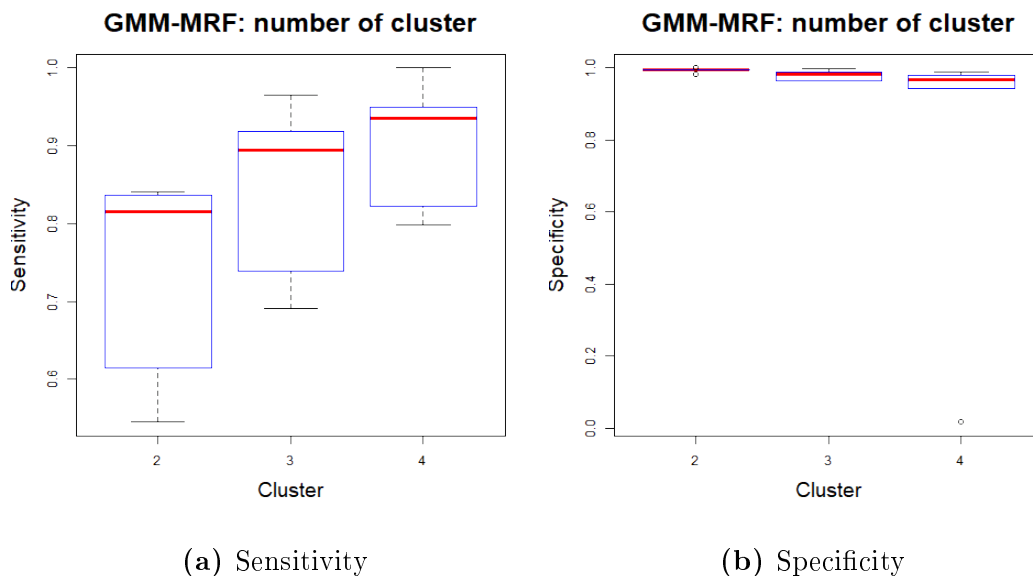**(d)** Accuracy

(e) DSC

Figure 4.5: GMM-MRF results: 3 cluster binarization threshold. Box plots of **(a)** Sensitivity, **(b)** Specificity, **(c)** Precision, **(d)** Accuracy and **(e)** DSC for the binarization threshold.

Sensitivity, accuracy and DSC show similar IQRs for both the binarization thresholds, but the threshold on the cluster 1 has a much higher median with respect the cluster 2 (0.89, 0.96 and 0.80 respectively). Specificity and Precision have slightly higher median values for the threshold 2 than the threshold 1, thus because of a high number of TN and TP with respect of FP.

4 cluster The figure 4.6 shows the boxplots of the evuoluation indices computed on the images segmented with GMM-MRF initialized with 4 clusters.
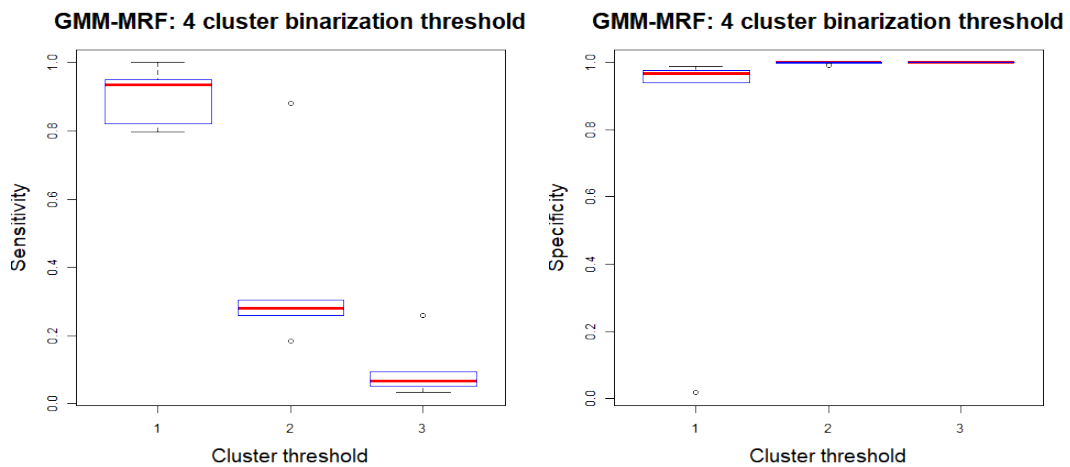
(a) Sensitivity
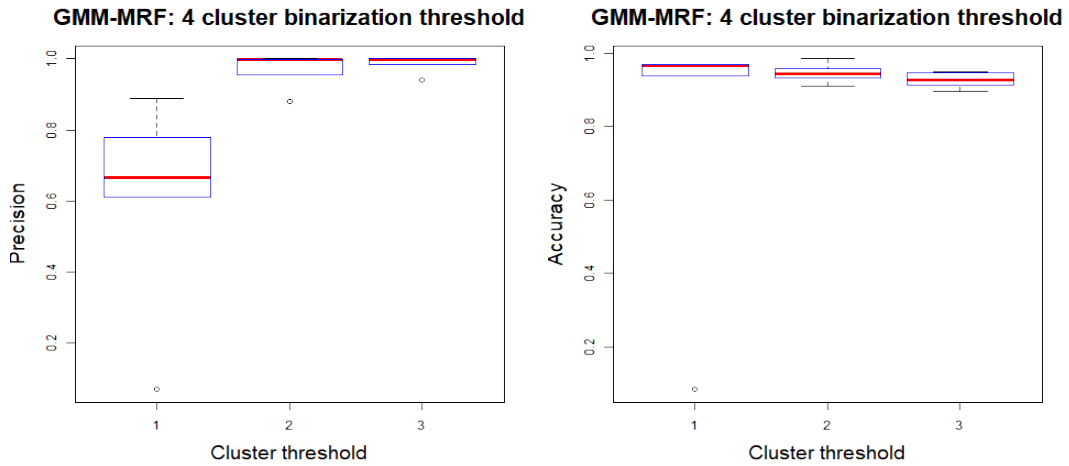
(b) Specificity

(c) Precision   **(d)** Accuracy

(e) DSC

Figure 4.6: GMM-MRF results: 4 cluster binarization threshold. Box plots of **(a)** Sensitivity, **(b)** Specificity, **(c)** Precision, **(d)** Accuracy and **(e)** DSC for the binarization threshold.

All the indices reported comparable IQRs for all the tested binarization thresholds; however, Sensitivity, Accuracy and DSC show very high median values for the threshold set on the cluster 1 (0.94, 0.96 and 0.78 respectively) with respect the other thresholds. The presence of a very high number of FN with respect the number of TP with a threshold on the cluster 3 cause the Sensitivity and the DSC to drop. The Specificity show all the thresholds with very high medians (~ 1). The Precision shows an outlier on all the thresholds, but the outlier of the threshold on cluster 1 causes a decreased median value with respect the other two.

Results GMM-MRF: number of cluster

The figure 4.7 shows the boxplots of the evualuation indices computed on the images segmented with GMM-MRF for the tuning of the number of cluster.

In all the indices the tested parameters show similar IQRs and high median values. With a number of cluster set to 2, the Specificity, Precision, Accuracy and DSC evaluation indices shows higher (but similar) median values with respect to the other tested parameter (median: 0.99, 0.91, 0.97 and 0.84 respectively). The lower values are with 4 clusters. However, with 2 clusters, the Sensitivity has a big IQR and a lower median with respect the other segmentations, showing a high number of FN with respect the TP. With 3 clusters the segmentations have pretty high median values for all the indices: Sensitivity 0.89, Specificity 0.98, Precision 0.77, Accuracy 0.96 and DSC 0.80, showing a low number of FN and FP with respect to the high number of TP and TN.
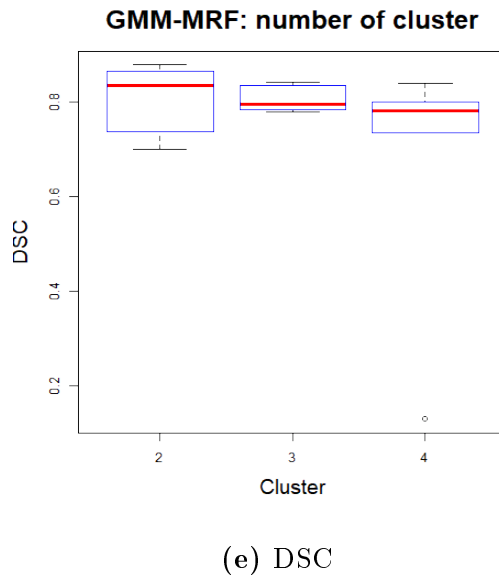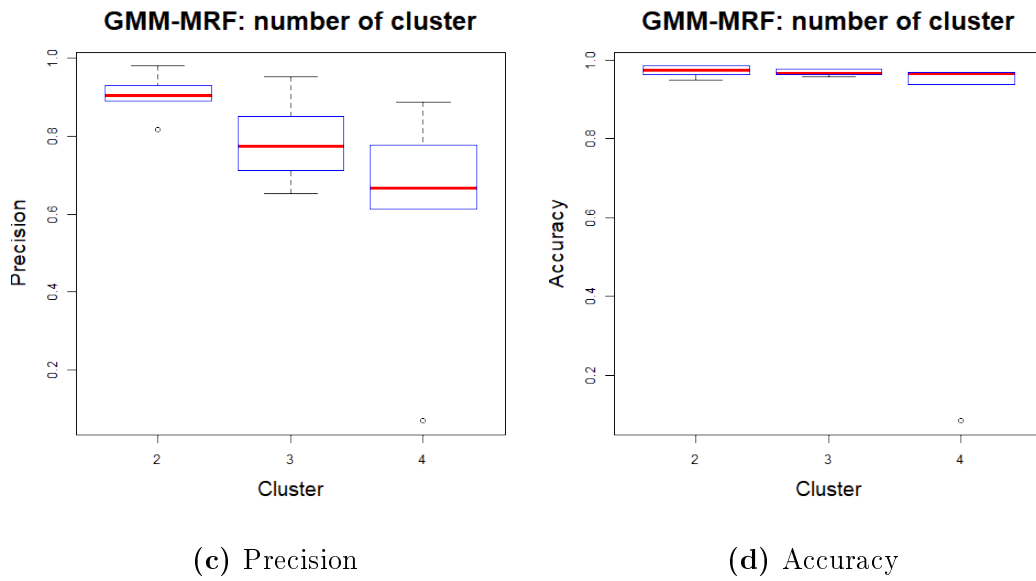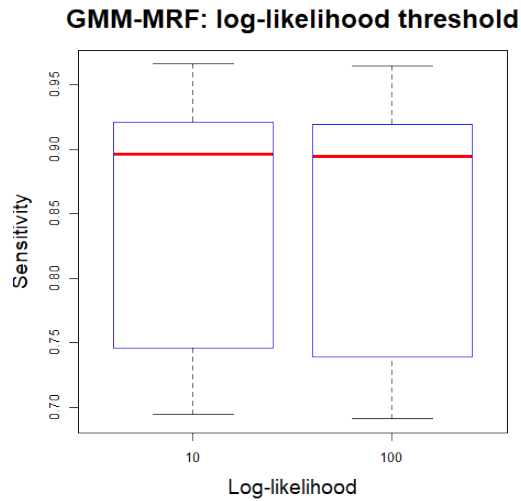

(a) Sensitivity

(b) Specificity

(c) Precision **(d)** Accuracy

(e) DSC

Figure 4.7: GMM-MRF results: number of cluster. Box plots of **(a)** Sensitivity, **(b)** Specificity, **(c)** Precision, **(d)** Accuracy and **(e)** DSC for the tuning of the number of cluster.
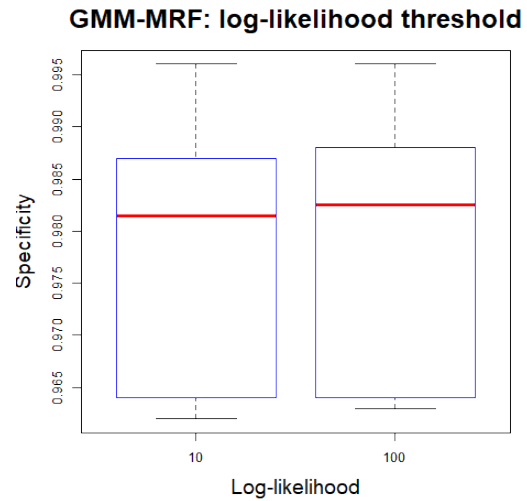
Results GMM-MRF: log-likelihood threshold

The figure 4.8 shows the boxplots of the evualuation indices computed on the images segmented with GMM-MRF for the tuning of the log-likelihood threshold.

All the indices have similar IQRs and median values for each one of the tested log-likelihood thresholds. The log-likelihood threshold set to 10 shows higher median value in Sensitivity and DSC (0.90 and 0.80 respectively). Specificity, Precision and Accuracy show almost equal median values for the tested parameters (0.98, 0.77 and 0.96 respectively).
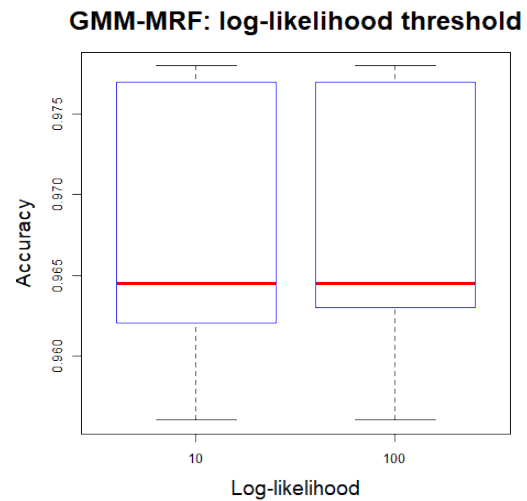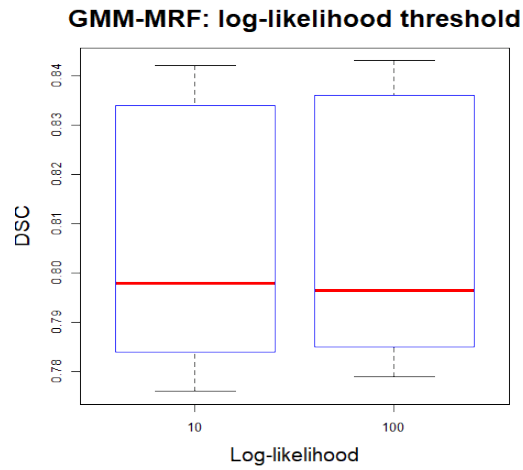

(a) Sensitivity

(b) Specificity
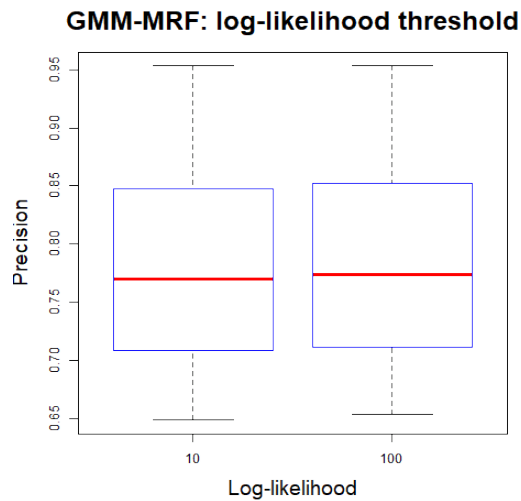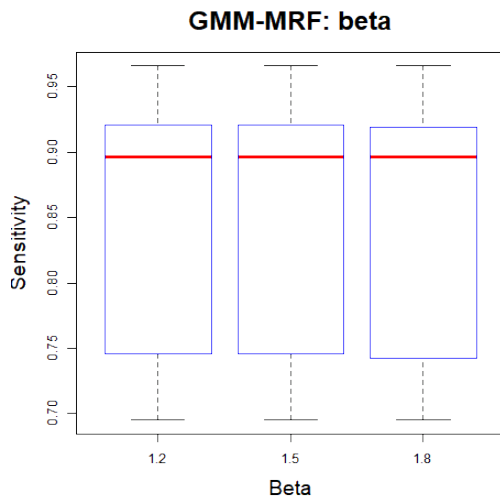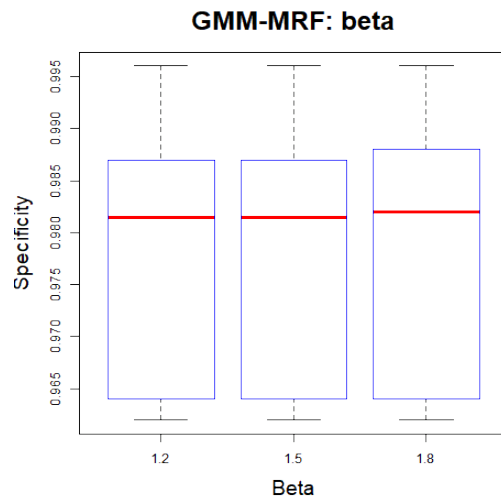

(c) Precision

(d) Accuracy

(e) DSC

Figure 4.8: GMM-MRF results: log-likelihood threshold. Box plots of **(a)** Sensitivity, **(b)** Specificity, **(c)** Precision, **(d)** Accuracy and **(e)** DSC for the tuning of the log-likelihood threshold.
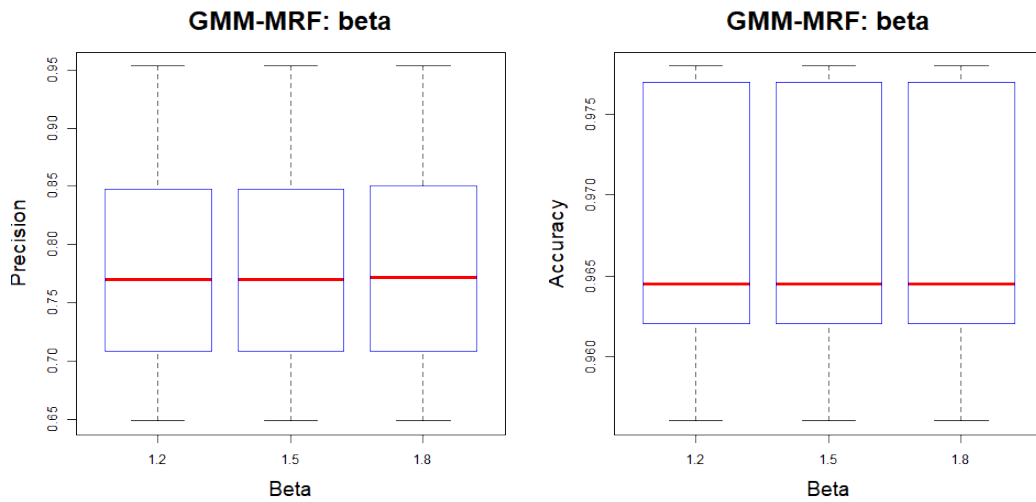
Results GMM-MRF: beta

The figure 4.9 shows the boxplots of the evualuation indices computed on the images segmented with GMM-MRF for the tuning of the beta value.

(a) Sensitivity

(b) Specificity

(c) Precision   **(d)** Accuracy

(e) DSC

Figure 4.9: GMM-MRF results: beta. Box plots of **(a)** Sensitivity, **(b)** Specificity, **(c)** Precision, **(d)** Accuracy and **(e)** DSC for the tuning of the beta value.

It does not show significant differences in all the indices even though changing the values of beta. All the indices have a very small IQR with a median value of Sensitivity, Specificity, Precision, Accuracy and DSC equal to 0.90, 0.98, 0.77, 0.96 and 0.80 respectively.

Results GMM-MRF: neighbourhood

The figure 4.10 shows the boxplots of the evuEation indices computed on the images segmented with GMM-MRF for the tuning of the neighbourhood value.
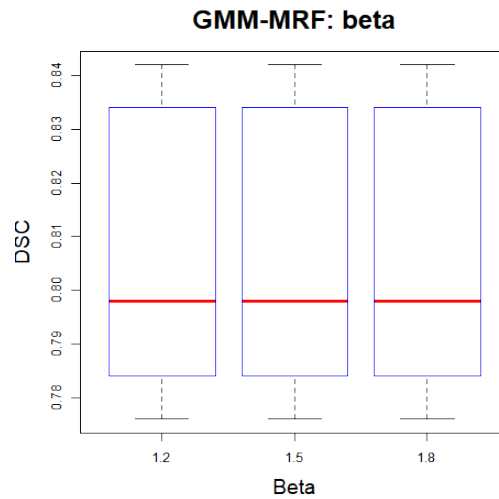
All the evaluation indices show slightly similar IQR and median values for both of the tested values of neighbourhood. However, Specificity, Precision and DSC have a higher median value with a neighbourhood of 26. Sensitivity and Accuracy have almost equal median values with 18 and 26 neighbouring voxels.
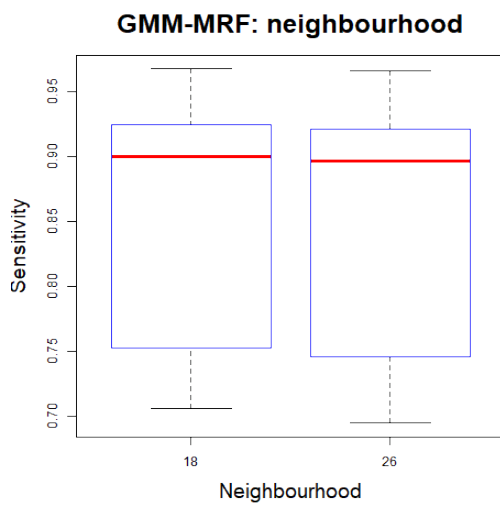
(a) Sensitivity
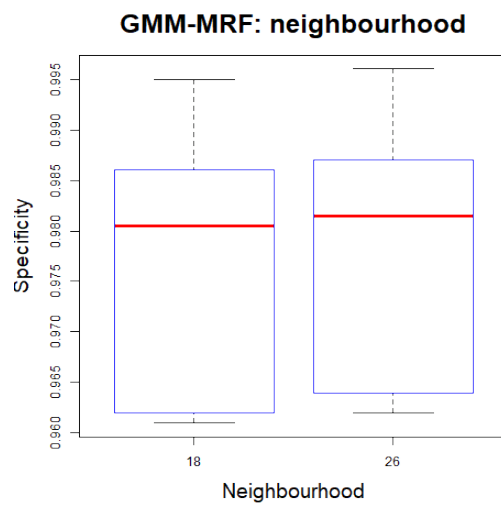
(b) Specificity
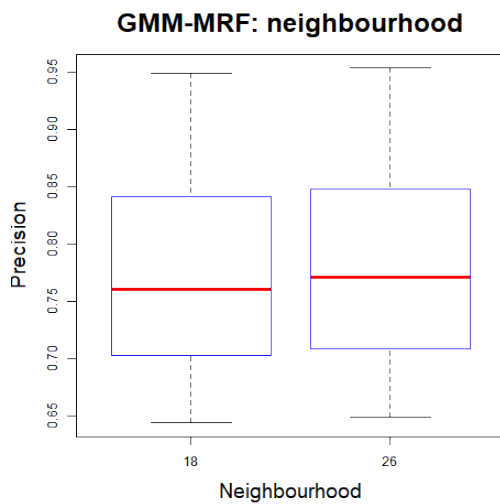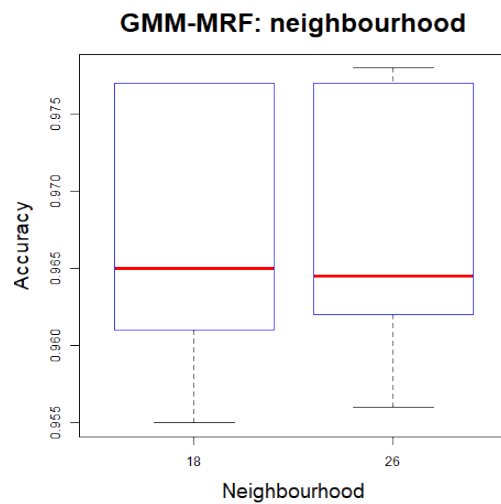
(c) Precision
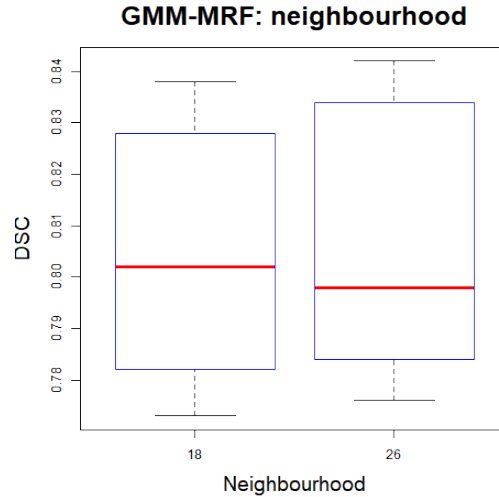
(d) Accuracy

(e) DSC

Figure 4.10: GMM-MRF results: neighbourhood. Box plots of **(a)** Sensitivity, **(b)** Specificity, **(c)** Precision, **(d)** Accuracy and **(e)** DSC for neighbourhood tuning.

4.2 Algorithm comparison results

This paragraph reports the results of the developed segmentation algorithms, using the parameter combinations tuned with the experiment described in section 3.2.4, and of the manual thresholding segmentation, in terms of Sensitivity, Specificity, Precision, Accuracy and DSC with respect to the ground truth dataset. It also reports the mean timing values of each segmentation method and a qualitative analysis of the different segmentation methods applied to a clinical volume.

The figure 4.11 shows the boxplots of the evusluation indices computed on the images segmented with manual threshold, GMM, GMM-MRF and GMM-MRF based on MIP methods with respect to the ground truth dataset.

The MIP segmentation has larger IQR with respect to the other methods in all the indices. The manual thresholding has very low values of Sensitivity, Precision and DSC, with a median value of 0.29, 0.12 and 0.16 respectively because of a high number and FN and FP with respect to the TP.

The GMM and GMM-MRF methods show similar IQRs, but the GMM has higher median values of Specificity and Precision ($\sim$ 1 and 0.92 respectively).

The GMM-MRF has the highest Sensitivity and DSC, with a median value of 0.90 and 0.80 respectively. It also has high values of Specificity and Accuracy (0.98 and 96 respectively), with an acceptable Precision (median 0.77).
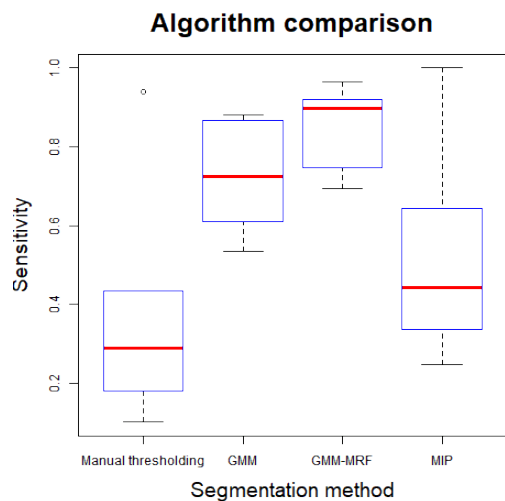
(a) Sensitivity

(b) Specificity
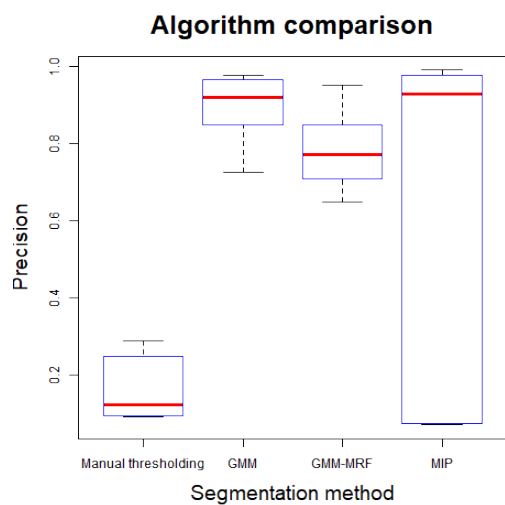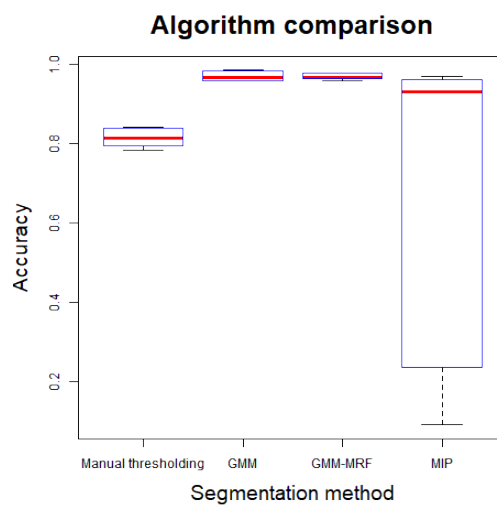
(c) Precision
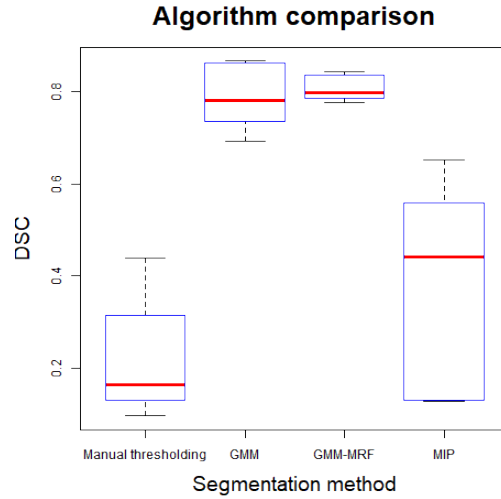
(d) Accuracy

(e) DSC

Figure 4.11: Algorithm comparison: evaluation indices. Box plots of **a** Specificity, **b** Sensitivity, **c** Precision, **d** Accuracy and **e** DSC computed on the images segmented with manual threshold, GMM, GMM-MRF and GMM-MRF based on MIP with respect to the ground truth dataset.

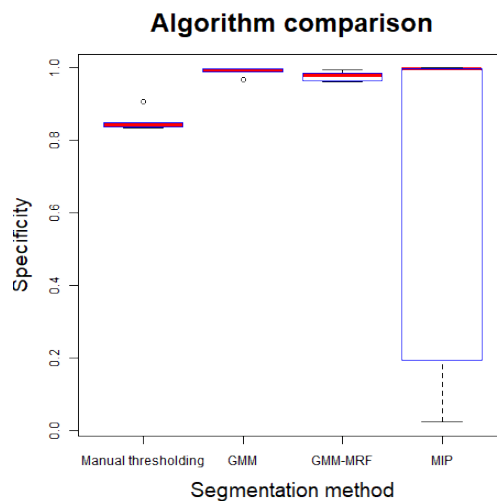With respect to the timing of each method, the table 4.12 show the results.

TIMING			
Manual threshold	**GMM**	**GMM-MRF**	**MIP**
Few minutes	100 ± 12 min	140 ± 10 min	56 ± 37 min

Figure 4.12: The table shows the timing of manual threshold, GMM, GMM-MRF and GMM-MRF based on MIP methods.

The manual thresholding requires at most few minutes (less than 5 minutes). On average, the GMM method requires $100 \pm 12min$ and the GMM-MRF requires $140 \pm 10min$ The GMM-MRF based on MIP requires $56 \pm 37min$.

The figure 4.13 shows the different segmentation methods applied to a clinical image.

(a) Original image

(b) Manual threshold

(c) GMM

(d) GMM-MRF

(e) MIP
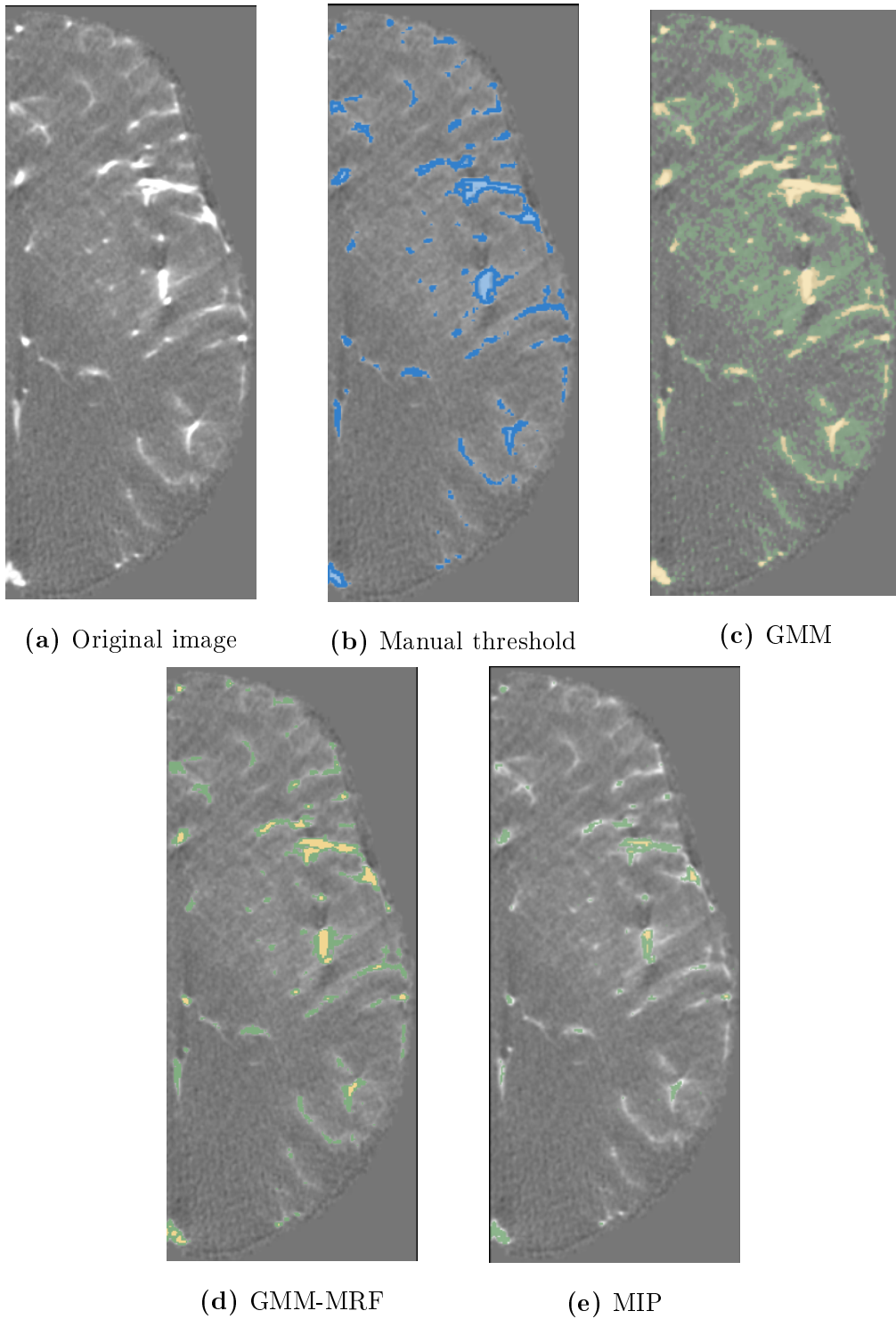
Figure 4.13: (**a**): Original image. (**b**): Manual thresholding segmentation. (**c**): GMM segmentation. (**d**): GMM-MRF segmentation. (**e**): GMM-MRF based on MIP segmentation.

We can see that, with respect the original slice (**a**):

- The manual threshold (**b**) in this example identifies correctly the larger vessels but it can't classify correctly the borders of the smallest vessels. A lower threshold results in increasing the number of FP and classifying noised areas as a whole vessel. Moreover it depends on the user.

- The GMM (**c**) over-estimates the vessels adding a lot of FP, especially in noised areas near vessels (Figure: 4.14).
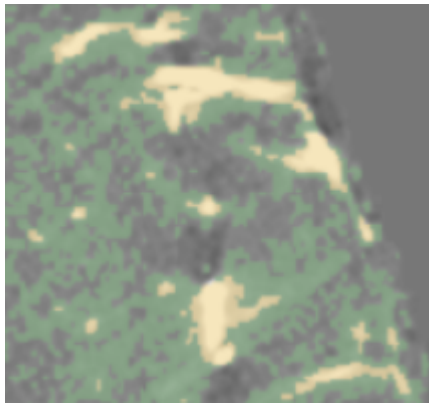
Figure 4.14: The figure shows a noised area that as been identified as a vessel structure by the GMM segmentation method.

- The GMM-MRF (**d**) classifies correctly both the large and small vessels with a high Accuracy also near branches diramations.

- The GMM-MRF based on MIP (**e**) under-estimates the vessel voxels. Thus, because the MIP are computed on the whole volume; this means that the projections along a direction where there is a high intricated vasculature, results in an image with high intensities distributed on the whole region of interest (Figure: 4.15), making harder the finding of vessel boundaries by the GMM-MRF algorithm and then resulting in a under-estimation of vessel structures.
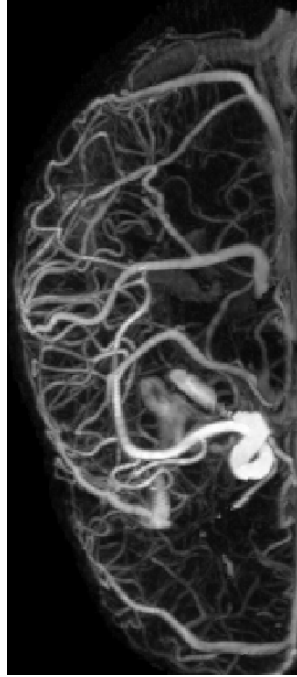
Figure 4.15: The figure shows a MIP on the whole volume along the axial direction.

Chapter 5

Discussion

This chapter will discuss the results of the experiments described in the previous sections and is divided into to parts:

- Discussion of the results of the tuning of the initialization parameters of both the GMM and GMM-MRF segmentation methods.

- Discussion of the results about the different segmentation algorithms with the correspondent tuned parameters.

5.1   Discussion: parameters tuning

The results of the experiments to tune the parameters of the GMM segmentation method reported in section 4.1 show that for 3 clusters, with the threshold on the cluster 1 (where 0 is the lowest mean cluster and 2 the highest), we have the highest Sensitivity (median value 0.99); thus, it means that, with respect to the ground truth data, it can recognize correctly the 99% of the voxel that belongs to the vessels; in fact the number of FN (so the voxels that belong to vessel structure but that are classified as background) is very low with respect to the TP. Despite that, with this threshold, the Precision and DSC indices dropped to very low values (0.25 and 0.40 respectively) because of a large amount of FP (voxels that are considered as *"vessel"* but that actually are *"background"*). Thus means that with such a threshold we classify too much voxels as vessels; so, for example, in a SEEG electrodes planning application, a lot of possible

trajectories will be rejected, thus reducing the effectiveness of the exam. Instead, the threshold on the cluster 2 has high values of Specificity (0.99), Precision (0.94), Accuracy (0.96) and DSC (0.77); the Sensitivity is a bit lower (median value 0.68) because a slightly higher number of FN that reduce the capability of the segmentation method to find the vessel with low intensities (that often correspond to the vessels of little diameter). For this reasons, for 3 clusters, the *selected threshold is on the cluster 2*, so the segmented images will consider the voxels that belongs to the cluster 2 as "vessel" and the cluster 0 and 1 as "background".

The experiments with 4 cluster show that, as the results for 3 clusters, the segmentations with the GMM method binarized with a threshold on the cluster 1 have a high overall Sensitivity because of the reduced FN, but very low values for all the other evaluation indices because the huge amount of FP voxels. Despite that, reducing the threshold on the cluster 3 results in the decreasing of the Sensitivity to a median value of 0.46, because of an increased number of FN. The threshold on the cluster 2 gives good results in terms of Sensitivity and Specificity (with median values of 0.96 and 0.91 respectively) with an overall accuracy of 0.92. For these reasons *we selected the threshold on the cluster 2* for 4 clusters. Thus, the selected threshold leads to a segmentation with a high number of FP but a reduced number of FN that means an overestimation of the voxels that belongs to vessel structures but at, the same time, the ability to identify correctly small vessels.

With the selected threshold for image binarization we tested the GMM segmentation method with a different number of cluster (2, 3 and 4). The results presented in paragraph 4.1.1 show that the segmentation with 3 clusters has higher Specificity, Precision, Accuracy and DSC (with the median values of 0.99, 0.94, 0.96 and 0.77 respectively) but with a lower Sensitivity with respect the segmentations with 2 and 4 clusters. The lower Sensitivity is caused by the high number of FN of two patients (patient 3 and patient 4). Despite that, looking at the vasculature models of a patient volume segmented with GMM with 2, 3 and 4 cluster (Figure 5.1), we can see that with 3 clusters we are able to identify more vessels. Thus, *we set the number of cluster to 3*.

(a) 2 Clusters

(b) 3 Clusters
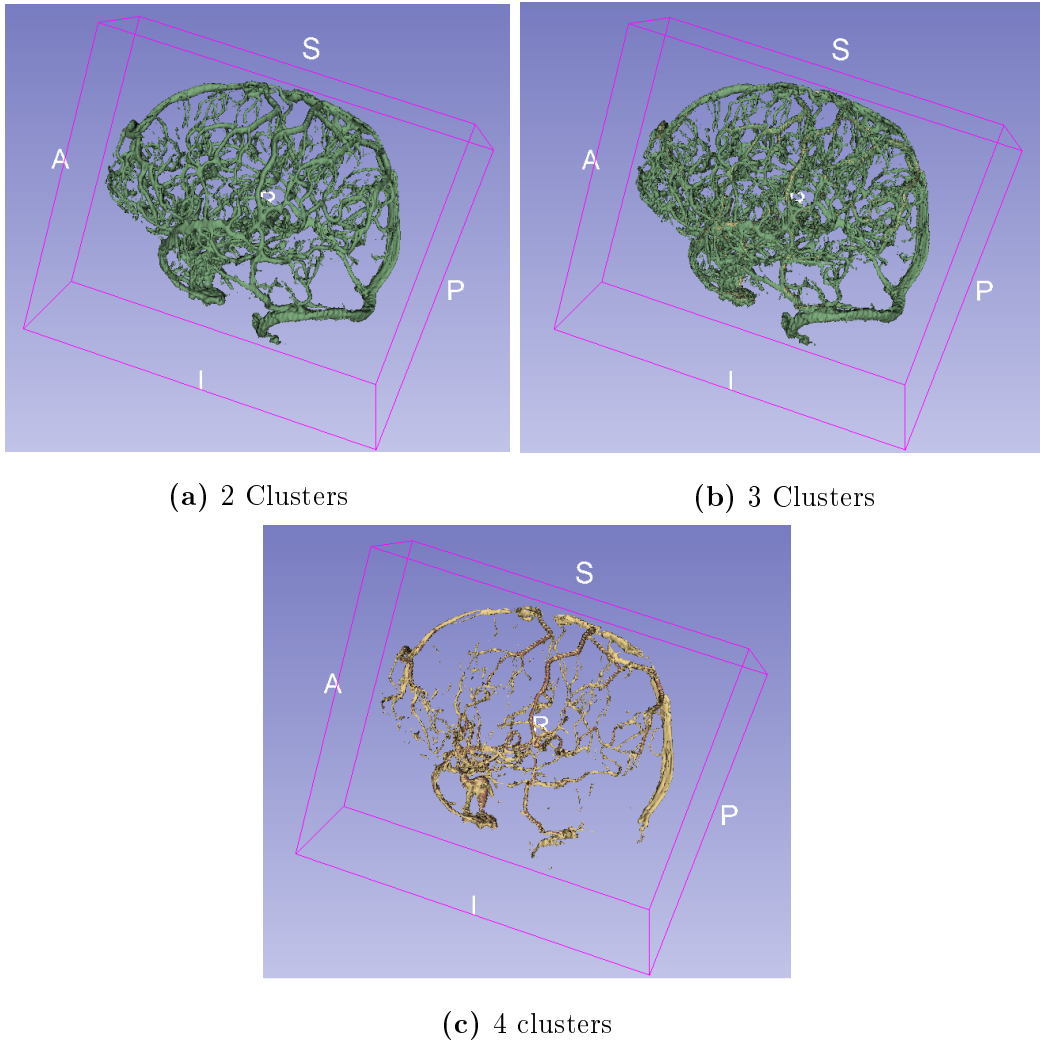
(c) 4 clusters

Figure 5.1: Vasculature models obtained in Slicer from the segmentation with (**a**): 2 clusters, (**b**): 3 clusters and (**c**): 4 clusters.

Analyzing the results reported in figure 4.4, we can see that setting the log-likelihood threshold to 10 the GMM segmentation method as the highest Sensitivity (median value 0.72), Accuracy (median value 0.97) and DSC (median value 0.78) with Specificity and Precision higher with a threshold set to 100.

We selected 10 as the log-likelihood threshold because it leads to a segmentation with a lower number of FN and a general high Accuracy in finding the vessel structures, even though it requires more time to converge.

In summary, the best combination of initialization parameters for the segmentation with the GMM technique is achieved with 3 cluster (binarized with a threshold on the cluster 2) and a log-likelihood threshold set to 10 (Figure: 5.2).

The results of the experiments to tune the parameters of the GMM-MRF segmentation method reported in section 4.1 show that, for 3 clusters, it is better to *select the binarization threshold on the cluster 1*; thus because it leads to high values of Sensitivity, Specificity, Accuracy and DSC (with a median value of 0.89, 0.98, 0.96 and 0.80 respectively) with respect the cluster 2 that has very low values of Sensitivity and DSC (0.19 and 0.32 respectively). It means a better identification of small vessels, due to few FN and a high number of TP and FP.

The experiments with 4 clusters have very low Sensitivity and DSC values for the binarization threshold set on the clusters 2 and 3. Thus, it means that with such thresholds the segmentation leads to very high numbers of FN, so a huge number of voxels, that belongs to vessel structures, are classified as background. Therefore, the selected *threshold is on the cluster 1*. It leads to the highest Sensitivity and DSC values (median values 0.94 and 0.78 respectively), with high Specificity and Accuracy but a lower Precision (with an acceptable median value though). Thus, it means that the algorithm tends to over-classify the voxels as vessel. For the automatic trajectory planning purpose, it is better to have more FP than FN to not damage important brain structures and to not harm the patients.

Looking at the figure 4.7 we can see that setting the number of cluster to 2, the segmetation has the highest values of Specificity, Precision, Accuracy and DSC (with median values of 0.99, 0.91, 0.97 and 0.84 respectively) but the lowest Sensitivity with a value of 0.82. Thus, it leads to an underestimation of the voxels that belong to vessels structure. Nevertheless, 4 clusters reduce the number of FN but increase the FP, thus leading to an over-segmentation. So, *we select 3 clusters* in order to have high Sensitivity (with a median value of 0.89) and high Specificity (with a median value of 0.98), reducing the number of FN and FP.

Looking at the figure 4.8, we can see that the results of each evaluation index are similar for all the patients. *We set the log-likelihood threshold to 10* because it has the highest Sensitivity (with a median value of 0.90) with the other indices comparable to the results with a threshold of 100. Thus, it means that the lower is the log-likelihood threshold, the better is the segmentation.

Analyzing the results reported in the figure 4.9, we can see that there is no significant

difference between the tested beta values (except for the Sensitivity and the Precision median values that are respectively slightly lower and slighlty higher with a beta of 1.8 with respect to the other tested values). Thus, *we set beta to 1.5* in order to have the highest values for all the indices.

The last tested parameter, the neighbourhood, has similar results for both the tested values (18 and 26). *We set the neighbourhood to 26* because it leads to a high Sensitivity value (almost equal to the resulting Sensitivity achieved with 18 neighbours) and to the highest values of each index, with very high Specificity and Accuracy values (0.98 and 0.97 respectively).

In summary, the best parameters configuration for the segmentation with the GMM-MRF method is achieved with 3 cluster (binarized with a threshold on the cluster 1), log-likelihood threshold set to 10, beta value of 1.5 and neighbourhood 26 (Figure: 5.2).

PARAMETERS CONFIGURATION					
Segmentation method	Cluster Threshold	Number of cluster	Log-likelihood threshold	Beta	Neighbourhood
GMM	2	3	10	1,5	26
GMM-MRF	1	3	10	1,5	26

Figure 5.2: The table shows best configuration of parameters for both the GMM and the GMM-MRF methods.

5.2 Discussion: algorithms comparison

The figure 4.11 shows that the GMM-MRF based on MIP has smaller values of Sensitivity, Specificity, Precision and Accuracy with respect the GMM and the GMM-MRF. Nevertheless it has better results with respect the manual thresholding.
Despite the GMM has high values of Specificity, Precision and Accuracy, the GMM-MRF has pretty similar indices (median values of 0.98, 0.77 and 0.96 respectively).
The GMM-MRF has the highest Sensitivity and DSC (median values of 0.90 and 0.80 respectively) because of a small number of FN and FP with respect the TP; thus, the segmentation does identify correctly also the vessels with a small caliber and classify

better the voxel on vessels boundaries.

In addition, in vessel segmentation for electrodes trajectroy planning, the higher the number of FN, the worse the effectiveness of the segmentation will be.

Looking at the timing results shown in table 4.12 we can see that the GMM-MRF based on MIP is the fastest segmentation method among the developed techniques. The GMM-MRF is the slowest method and it takes more than two hours, but the obtained segmentation images worth the timing.

In conclusion we can assert that the GMM-MRF segmentation methods shows the best results in terms of Sensitivity, Specificity and Accuracy with the configuration of parameters summarized in the table 5.2. It can classify correctly both large and small vessels as can be seen in figure 4.13. In addition, the timing respects the specifications.
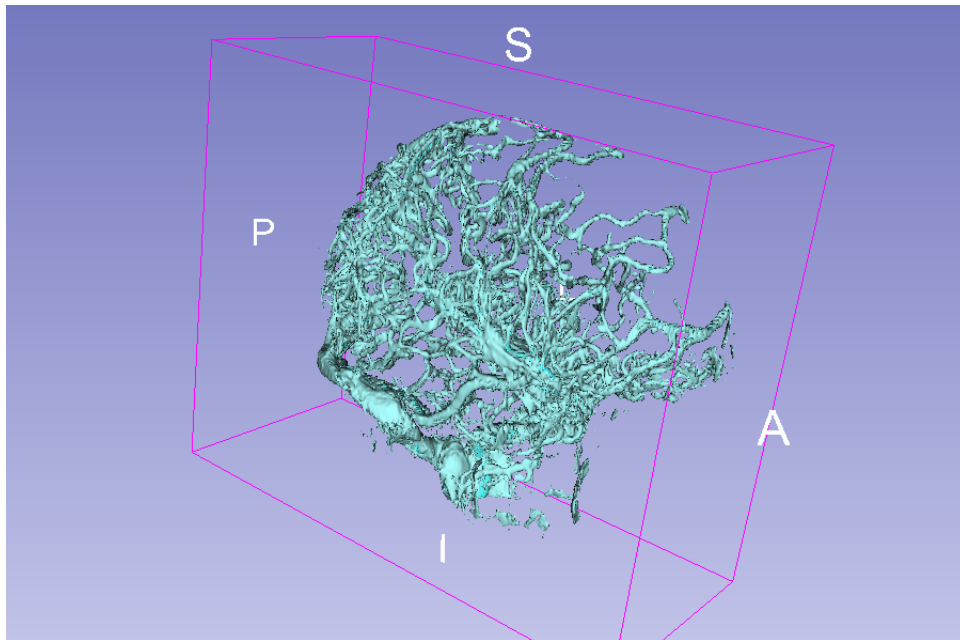

Figure 5.3: The figure shows the vasculature model obtained after the segmentation with the GMM-MRF.

Chapter 6

Conclusions

For patients with medically refractory focal epilepsy, that can't be treated with anti-epileptical drugs and are considered to have a reasonable chance of progressing to potentially curative surgery, the stereo-electroencephalography (SEEG) is a solution to localize the epileptogenic zone when the non-invasive methods fails. The SEEG is a diagnostic procedure in which multiple intracranial depth electrodes are placed to record electrical activity in selected cortical and subcortical structures. Thus, the planning of the trajectories is a very risky and complicated procedure because it has to find the shortest trajectory between the entry points and the target points while avoiding important brain structures such as vessel.

The vessel avoidance is one of the most important constraint and, to compute the distance between the electrode trajectories and the vessels, the first step is to segment the vasculature inside the volume of interest.

This work focused on the development and comparison of different completely automatic methods based on the Gaussian mixture model (GMM) to improve the automated planning workflow described in [36]. In particular, we developed the GMM and the GMM with Markov Random Fields (MRF) that introduces a classification correction of the voxel basing on their neighbouring voxels. Furthermore, we developed the GMM-MRF applied on iterative Maximum Intensity Projections (MIPs) of the whole volume as described in [15], to test its performance on real brain vessel segmentation.

This work is able to improve the planning workflow described in section 2.2.5: the brain vessel segmentation of 3D CBCT DSA images was done only with a manual

intensity-based thresholding, but this method is user-dependant and, despite the rapidity, it leads to planification problems, especially in case of noised dataset.

After the tuning of the initialization parameters of all the developed segmentation methods, the results show that the GMM-MRF algorithm leads to better segmentations than the manual thresholding and the other developed methods. This technique has high Sensitivity and Accuracy thanks to the analysis of the neighbouring voxels, that ensures the correct classification of vessels with both small and large diameter. Therefore, it is precise also near branching diramations, where the manual threshold tends to fail.

Chapter 7

Actual limits and future developments

The limited dataset weakens the significance of the results that are not supported by a statistical analysis. A future development can be the increasing of available dataset images with the correspondent ground truth in order to support the results with a statistical significance.

The GMM-MRF based on MIP has shown a great potential in terms of timing and fine classification of vessels, but the MIP images on the whole volume decrease the performance of this method.

The method can improve if the MIP are generated on smaller volumes; a solution can be to iterate the method on MIPs created with little portion of the volume (such as slab of 10 to 15 slices) in order to reduce the super-imposition of the voxels with highest intensities and improving the ability of GMM-MRF classification.

The implemented segmentation methods could be tested also with MR images in order to verify which clinical data lead to the best results with the automated planner.

Bibliography

[1] A. M. Mendrik * et al. "Noise Reduction in Computed Tomography Scans Using 3-D Anisotropic Hybrid Diffusion With Continuous Switch". In: *IEEE Transactions on Medical Imaging* 28.10 (Oct. 2009), pp. 1585–1594. ISSN: 0278-0062. DOI: `10.1109/TMI.2009.2022368`.

[2] R. Adams and L. Bischof. "Seeded Region Growing". In: *IEEE Trans. Pattern Anal. Mach. Intell.* 16.6 (June 1994), pp. 641–647. ISSN: 0162-8828. DOI: `10.1109/34.295913`. URL: `http://dx.doi.org/10.1109/34.295913`.

[3] S. A. Ahmadi et al. "Advanced planning and intra-operative validation for robot-assisted keyhole neurosurgery In ROBOCAST". In: *2009 International Conference on Advanced Robotics*. June 2009, pp. 1–7.

[4] Ravindra Arya et al. "Adverse events related to extraoperative invasive EEG monitoring with subdural grid electrodes: A systematic review and meta-analysis". In: *Epilepsia* 54.5 (May 2013), pp. 828–839. ISSN: 1528-1167. DOI: `10.1111/epi.12073`. URL: `http:https://doi.org/10.1111/epi.12073`.

[5] Christopher M Bishop. *Pattern recognition and machine learning.* springer, 2006.

[6] Francesco Cardinale et al. "Cerebral Angiography for Multimodal Surgical Planning in Epilepsy Surgery: Description of a New Three-Dimensional Technique and Literature Review." eng. In: *World neurosurgery* 84 (2 Aug. 2015), pp. 358–67.

[7] Francesco Cardinale et al. "Stereoelectroencephalography: surgical methodology, safety, and stereotactic application accuracy in 500 procedures." eng. In: *Neurosurgery* 72 (3 Mar. 2013), 353–66, discussion 366.

[8] S. Chaudhuri et al. "Detection of blood vessels in retinal images using two-dimensional matched filters". In: *IEEE Transactions on Medical Imaging* 8.3 (Sept. 1989), pp. 263–269. ISSN: 0278-0062. DOI: 10.1109/42.34715.

[9] Massimo Cossu et al. "Epilepsy surgery in children: results and predictors of outcome on seizures." eng. In: *Epilepsia* 49 (1 Jan. 2008), pp. 65–72.

[10] E. De Momi et al. "Multi-trajectories automatic planner for StereoElectroEncephaloGraphy (SEEG)". In: *International Journal of Computer Assisted Radiology and Surgery* 9.6 (Nov. 2014), pp. 1087–1097. ISSN: 1861-6429. DOI: 10.1007/s11548-014-1004-1. URL: https://doi.org/10.1007/s11548-014-1004-1.

[11] Maryam Taghizadeh Dehkordi, Saeed Sadri, and Alimohamad Doosthoseini. *A Review of Coronary Vessel Segmentation Algorithms*. eng. India, Jan. 2011.

[12] John S. Duncan. "Imaging in the surgical treatment of epilepsy". In: *Nat Rev Neurol* 6.10 (Oct. 2010), pp. 537–550. ISSN: 1759-4758. URL: http://dx.doi.org/10.1038/nrneurol.2010.131.

[13] Robert S. Fisher et al. "ILAE Official Report: A practical clinical definition of epilepsy". In: *Epilepsia* 55.4 (2014), pp. 475–482. ISSN: 1528-1167. DOI: 10.1111/epi.12550. URL: http://dx.doi.org/10.1111/epi.12550.

[14] Alejandro F. Frangi et al. "Multiscale vessel enhancement filtering". In: *Medical Image Computing and Computer-Assisted Intervention — MICCAI'98: First International Conference Cambridge, MA, USA, October 11–13, 1998 Proceedings*. Ed. by William M. Wells, Alan Colchester, and Scott Delp. Berlin, Heidelberg: Springer Berlin Heidelberg, 1998, pp. 130–137. ISBN: 978-3-540-49563-5. DOI: 10.1007/BFb0056195. URL: https://doi.org/10.1007/BFb0056195.

[15] Rui Gan, Wilbur C. K. Wong, and Albert C. S. Chung. "Statistical cerebrovascular segmentation in three-dimensional rotational angiography based on maximum intensity projections". In: *Medical Physics* 32.9 (2005), pp. 3017–3028. ISSN: 2473-4209. DOI: 10.1118/1.2001820. URL: http://dx.doi.org/10.1118/1.2001820.

[16] Jorge Gonzalez-Martinez et al. "Stereotactic placement of depth electrodes in medically intractable epilepsy". In: *Journal of Neurosurgery* 120.3 (2014). PMID: 24405074, pp. 639–644. DOI: 10.3171/2013.11.JNS13635. eprint: https://doi.org/10.3171/2013.11.JNS13635. URL: https://doi.org/10.3171/2013.11.JNS13635.

[17] Gregory L. Holmes and Yezekiel Ben-Ari. "Seizing hold of seizures". In: *Nat Med* 9.8 (Aug. 2003), pp. 994–996. ISSN: 1078-8956. URL: http://dx.doi.org/10.1038/nm0803-994.

[18] Tina Kapur et al. "Increasing the impact of medical image computing using community-based open-access hackathons: The NA-MIC and 3D Slicer experience". In: *Medical Image Analysis* 33 (2016). 20th anniversary of the Medical Image Analysis journal (MedIA), pp. 176–180. ISSN: 1361-8415. DOI: http://dx.doi.org/10.1016/j.media.2016.06.035. URL: http://www.sciencedirect.com/science/article/pii/S1361841516301128.

[19] Michael Kass, Andrew Witkin, and Demetri Terzopoulos. "Snakes: Active contour models". In: *International Journal of Computer Vision* 1.4 (Jan. 1988), pp. 321–331. ISSN: 1573-1405. DOI: 10.1007/BF00133570. URL: https://doi.org/10.1007/BF00133570.

[20] Patrick Kwan and Martin J Brodie. "Drug treatment of epilepsy: when does it fail and how to optimize its use?" In: *CNS spectrums* 9.2 (2004), pp. 110–119.

[21] George L. Turin. "An Introduction to Matched Filters". In: IT-6 (July 1960), pp. 311–329.

[22] P. Liskowski and K. Krawiec. "Segmenting Retinal Blood Vessels With Deep Neural Networks". In: *IEEE Transactions on Medical Imaging* 35.11 (Nov. 2016), pp. 2369–2380. ISSN: 0278-0062. DOI: 10.1109/TMI.2016.2546227.

[23] William E. Lorensen and Harvey E. Cline. "Marching Cubes: A High Resolution 3D Surface Construction Algorithm". In: *SIGGRAPH Comput. Graph.* 21.4 (Aug. 1987), pp. 163–169. ISSN: 0097-8930. DOI: 10.1145/37402.37422. URL: http://doi.acm.org/10.1145/37402.37422.

[24] H. Matsumoto and C. Ajmone Marsan. "Cellular Mechanisms in Experimental Epileptic Seizures". In: *Science* 144.3615 (1964), pp. 193–194. ISSN: 0036-8075. DOI: `10.1126/science.144.3615.193`. eprint: `http://science.sciencemag.org/content/144/3615/193.full.pdf`. URL: `http://science.sciencemag.org/content/144/3615/193`.

[25] Andrew Mehnert and Paul Jackway. "An improved seeded region growing algorithm". In: *Pattern Recognition Letters* 18.10 (1997), pp. 1065–1071. ISSN: 0167-8655. DOI: `http://dx.doi.org/10.1016/S0167-8655(97)00131-1`. URL: `http://www.sciencedirect.com/science/article/pii/S0167865597001311`.

[26] F. Meyer and S. Beucher. "Morphological segmentation". In: *Journal of Visual Communication and Image Representation* 1.1 (1990), pp. 21–46. ISSN: 1047-3203. DOI: `http://dx.doi.org/10.1016/1047-3203(90)90014-M`. URL: `http://www.sciencedirect.com/science/article/pii/104732039090014M`.

[27] E. De Momi et al. "Automatic Trajectory Planner for StereoElectroEncephaloGraphy Procedures: A Retrospective Study". In: *IEEE Transactions on Biomedical Engineering* 60.4 (Apr. 2013), pp. 986–993. ISSN: 0018-9294. DOI: `10.1109/TBME.2012.2231681`.

[28] D.T Morris and C Donnison. "Identifying the neuroretinal rim boundary using dynamic contours". In: *Image and Vision Computing* 17.3 (1999), pp. 169–174. ISSN: 0262-8856. DOI: `http://dx.doi.org/10.1016/S0262-8856(98)00093-6`. URL: `http://www.sciencedirect.com/science/article/pii/S0262885698000936`.

[29] C. Munari et al. "Stereo-electroencephalography methodology: advantages and limits". In: *Acta Neurologica Scandinavica* 89.S152 (Mar. 1994), pp. 56–67. ISSN: 1600-0404. DOI: `10.1111/j.1600-0404.1994.tb05188.x`. URL: `http:https://doi.org/10.1111/j.1600-0404.1994.tb05188.x`.

[30] N. Nguyen, Q. M. J. Wu, and S. Ahuja. "An Extension of the Standard Mixture Model for Image Segmentation". In: *IEEE Transactions on Neural Networks* 21.8 (Aug. 2010), pp. 1326–1338. ISSN: 1045-9227. DOI: `10.1109/TNN.2010.2054109`.

[31]   Çagatay Önal et al. "Complications of invasive subdural grid monitoring in chil-
        dren with epilepsy". In: *Journal of Neurosurgery* 98.5 (2003). PMID: 12744361,
        pp. 1017–1026. DOI: `10.3171/jns.2003.98.5.1017`. eprint: `https://doi.org/`
        `10.3171/jns.2003.98.5.1017`. URL: `https://doi.org/10.3171/jns.2003.`
        `98.5.1017`.

[32]   Douglas Reynolds. "Gaussian Mixture Models". In: *Encyclopedia of Biometrics.*
        Ed. by Stan Z. Li and Anil Jain. Boston, MA: Springer US, 2009, pp. 659–663.
        ISBN: 978-0-387-73003-5. DOI: `10.1007/978-0-387-73003-5_196`. URL: `https:`
        `//doi.org/10.1007/978-0-387-73003-5_196`.

[33]   Jonathan C. Roberts. *An Overview of Rendering from Volume Data - including
        Surface and Volume Rendering.* Tech. rep. 1993.

[34]   Yoshinobu Sato et al. "Three-dimensional multi-scale line filter for segmentation
        and visualization of curvilinear structures in medical images". In: *Medical Image
        Analysis* 2.2 (1998), pp. 143–168. ISSN: 1361-8415. DOI: `http://dx.doi.org/`
        `10.1016/S1361-8415(98)80009-1`. URL: `http://www.sciencedirect.com/`
        `science/article/pii/S1361841598800091`.

[35]   Ingrid E. Scheffer et al. "ILAE classification of the epilepsies: Position paper of
        the ILAE Commission for Classification and Terminology". In: *Epilepsia* 58.4
        (Apr. 2017), pp. 512–521. ISSN: 1528-1167. DOI: `10.1111/epi.13709`. URL:
        `http:https://doi.org/10.1111/epi.13709`.

[36]   Davide Scorza et al. "Retrospective evaluation and SEEG trajectory analysis
        for interactive multi-trajectory planner assistant". In: *International Journal of
        Computer Assisted Radiology and Surgery* (July 2017). ISSN: 1861-6429. DOI:
        `10.1007/s11548-017-1641-2`. URL: `https://doi.org/10.1007/s11548-017-`
        `1641-2`.

[37]   Reuben R. Shamir et al. "Reduced risk trajectory planning in image-guided key-
        hole neurosurgery". In: *Medical Physics* 39.5 (2012), pp. 2885–2895. ISSN: 2473-
        4209. DOI: `10.1118/1.4704643`. URL: `http://dx.doi.org/10.1118/1.`
        `4704643`.

[38] Rachel Sparks et al. "Automated multiple trajectory planning algorithm for the placement of stereo-electroencephalography (SEEG) electrodes in epilepsy treatment". In: *International Journal of Computer Assisted Radiology and Surgery* 12.1 (Jan. 2017), pp. 123–136. ISSN: 1861-6429. DOI: 10.1007/s11548-016-1452-x. URL: https://doi.org/10.1007/s11548-016-1452-x.

[39] Rachel Sparks et al. "Efficient Anatomy Driven Automated Multiple Trajectory Planning for Intracranial Electrode Implantation". In: *Medical Image Computing and Computer-Assisted Intervention – MICCAI 2016: 19th International Conference, Athens, Greece, October 17-21, 2016, Proceedings, Part I.* Ed. by Sebastien Ourselin et al. Cham: Springer International Publishing, 2016, pp. 542–550. ISBN: 978-3-319-46720-7. DOI: 10.1007/978-3-319-46720-7_63. URL: https://doi.org/10.1007/978-3-319-46720-7_63.

[40] Khoa Anh Tran et al. "Gaussian Mixture Model Based on Hidden Markov Random Field for Color Image Segmentation". In: *Ubiquitous Information Technologies and Applications: CUTE 2013.* Ed. by Young-Sik Jeong et al. Berlin, Heidelberg: Springer Berlin Heidelberg, 2014, pp. 189–197. ISBN: 978-3-642-41671-2. DOI: 10.1007/978-3-642-41671-2_25. URL: https://doi.org/10.1007/978-3-642-41671-2_25.

[41] Jamie J. Van Gompel et al. "INTRACRANIAL ELECTROENCEPHALOGRAPHY WITH SUBDURAL GRID ELECTRODESTECHNIQUES, COMPLICATIONS, AND OUTCOMES". In: *Neurosurgery* 63.3 (2008), pp. 498–506. DOI: 10.1227/01.NEU.0000324996.37228.F8. eprint: /oup/backfile/content_public/journal/neurosurgery/63/3/10.1227_01.neu.0000324996.37228.f8/2/neurosurgery-63-3-498.pdf. URL: +%20http://dx.doi.org/10.1227/01.NEU.0000324996.37228.F8.

[42] Joachim Weickert. "A review of nonlinear diffusion filtering". In: *Scale-Space Theory in Computer Vision: First International Conference, Scale-Space'97 Utrecht, The Netherlands, July 2–4, 1997 Proceedings.* Ed. by Bart ter Haar Romeny et al. Berlin, Heidelberg: Springer Berlin Heidelberg, 1997, pp. 1–28. ISBN: 978-3-540-

69196-9. DOI: 10.1007/3-540-63167-4_37. URL: https://doi.org/10.1007/3-540-63167-4_37.

[43]   Rina Zelmann et al. "Automatic optimization of depth electrode trajectory planning". In: *Workshop on Clinical Image-Based Procedures*. Springer. 2013, pp. 99–107.

[44]   Bob Zhang et al. "Retinal vessel extraction by matched filter with first-order derivative of Gaussian". In: *Computers in Biology and Medicine* 40.4 (2010), pp. 438–445. ISSN: 0010-4825. DOI: http://dx.doi.org/10.1016/j.compbiomed.2010.02.008. URL: http://www.sciencedirect.com/science/article/pii/S0010482510000302.

[45]   G. Zombori et al. "A Computer Assisted Planning System for the Placement of sEEG Electrodes in the Treatment of Epilepsy". In: *Information Processing in Computer-Assisted Interventions: 5th International Conference, IPCAI 2014, Fukuoka, Japan, June 28, 2014. Proceedings.* Ed. by Danail Stoyanov et al. Cham: Springer International Publishing, 2014, pp. 118–127. ISBN: 978-3-319-07521-1. DOI: 10.1007/978-3-319-07521-1_13. URL: https://doi.org/10.1007/978-3-319-07521-1_13.

[46]   Maria A. Zuluaga et al. "Stability, structure and scale: improvements in multi-modal vessel extraction for SEEG trajectory planning". In: *International Journal of Computer Assisted Radiology and Surgery* 10.8 (Aug. 2015), pp. 1227–1237. ISSN: 1861-6429. DOI: 10.1007/s11548-015-1174-5. URL: https://doi.org/10.1007/s11548-015-1174-5.

[47]   Dominik Zumsteg and Heinz Gregor Wieser. "Presurgical Evaluation: Current Role of Invasive EEG". In: *Epilepsia* 41.s3 (Mar. 2000), S55–S60. ISSN: 1528-1167. DOI: 10.1111/j.1528-1157.2000.tb01535.x. URL: http:https://doi.org/10.1111/j.1528-1157.2000.tb01535.x.